Helioseismic and Magnetic Imager
Calibration and Measurement Algorithms Document

HMI-CMAD-0001
First draft

Prepared by
Charles Baldner and the HMI team

Effective date: July 13, 2023

Signature Page
Helioseismic and Magnetic Imager
Calibration and Measurement Algorithms Document
HMI-CMAD-0001

J. Todd Hoeksema	Date
HMI SIT Principal Investigator	
Charles Baldner	Date
HMI Instrument Scientist	

By signing this document, signatories are certifying that the content herein is acceptable direction for managing the project's data and that they will ensure its implementation by those over whom they have authority.

Calibration and Algorithms Document

CHANGE HISTORY LOG
Sheet: 1 of 1

Revision	Effective Date	Description of changes
First draft	July 13, 2023	First draft of HMI CMAD

Contents

1 Scope

The Calibration and Measurement Algorithm Documents (CMADs) for the Helioseismic and Magnetic Imager (HMI, Scherrer, J. Schou, et al., 2012; J. Schou, Scherrer, et al., 2012) on the Solar Dynamics Observatory (SDO, Pesnell, Thompson, and Chamberlin, 2012) describe the overall calibration concept for the instrument and the algorithms used to convert observed images from the instrument into the various scientific data products and quantities HMI provides to the solar physics community and broader public. Described herein are the performance requirements and error budgets for all relevant subsystems, the pre-flight and in-flight calibration measurements made, and the algorithms used to apply them to the data. Further, the algorithms used to compute HMI's data products are described: images of line-of-sight velocity, line-of-sight and full vector magnetic field, continuum intensity, power spectra, helioseismic parameter estimation, sub-surface flow velocities, among others. Uncertainties and systematic errors are discussed, and where possible quantitative error estimates are made or described. Brief descriptions are given of the instrument's scientific program, and its design and heritage, but are described more fully in other documents. Where relevant to data calibration, on orbit performance and trending are also discussed. Detailed discussions of the instrument's operation, overall on-orbit performance, and data processing and delivery are given in other documents. Because of the number of distinct data products produced by HMI, many with largely unrelated algorithms, the HMI CMAD documentation is divided into a number of separate documents.

This first document describes the calibrations applied to the observed images (referred to henceforth as 'filtergrams') before they are used in higher level data products, and describes the generation of the basic science data products, the line-of-sight quantities or "observables". The full list of CMADs is given in section 2.2.

2 Related Documentations

2.1 Applicable Documents

The following documents include proposals, plans, and specifications from the design, construction, and testing phases of the instrument, and were valid on the dates indicated. Where conflicts exist, this document supersedes those listed here.

Document Number	Title	Date
HMI-S013	Instrument Performance Document	2004.11.03
HMI-S014	HMI Science Plan & Requirements	2004.11.04
HMI-S020	HMI Instrument Calibration Plan	
HMI-S028	Ground Calibration Documents	2006.12.08
HMI-S029	HMI Filter Calibration Plan	2006.12.11
HMI-S030	HMI Polarization Calibration Plan	2006.12.11

2.2   HMI CMAD documents

CMAD Document Name	Description
Basic Data Products	(This document) Ground and in-flight calibration of filtergrams and Stokes components, and generation of LOS observables (Doppler velocity, LOS magnetic flux density, etc.)
Vector Magnetic Field	Milne-Eddington inversion for full vector magnetic field
Local Helioseismology	Region tracking, power spectrum generation, mode parameter estimation, and flow inversions
Global Helioseismology	Spherical harmonic time series generation and power spectra, mode parameter estimation and rotation inversions
HARPS/SHARPS	Active region detection and characterization

3   Overview and Background Information

3.1   Science Objectives

The primary science goal of the HMI instrument is to "study the origin of solar variability and to characterize and understand the Sun's interior and the various components of magnetic activity."[1] As part of NASA's flagship Living With A Star (LWS) mission, HMI is also intended to study how the Sun drives space weather, and to help develop and improve predictive methods for solar phenomena that influence space weather and human activities on and near Earth. The science objectives rely on synoptic measurements of physical quantities of the Sun that can be determined using spectropolarimetry. Figure 1 provides a schematic concept of the HMI analysis pipeline showing how filtergrams are processed to provide quantitative physical observables and then higher level products that inform the SDO science investigations.

3.2   HMI Instrument Description

As the instrument's name suggests, there are two broad components to the instrument's scientific program: helioseismic observations, and magnetic field measurements. To achieve both these goals, HMI produces high time cadence, high spatial resolution, extremely narrow bandpass images at selectable wavelengths and polarization states, centered on the Fe I absorption line at 6173 Å. These images are transmitted to the ground, where they are calibrated and used to compute HMI's science data products. The primary data products needed to achieve HMI's science goals are full disk resolved measurements of the photospheric velocity along the observers line of sight, and full disk
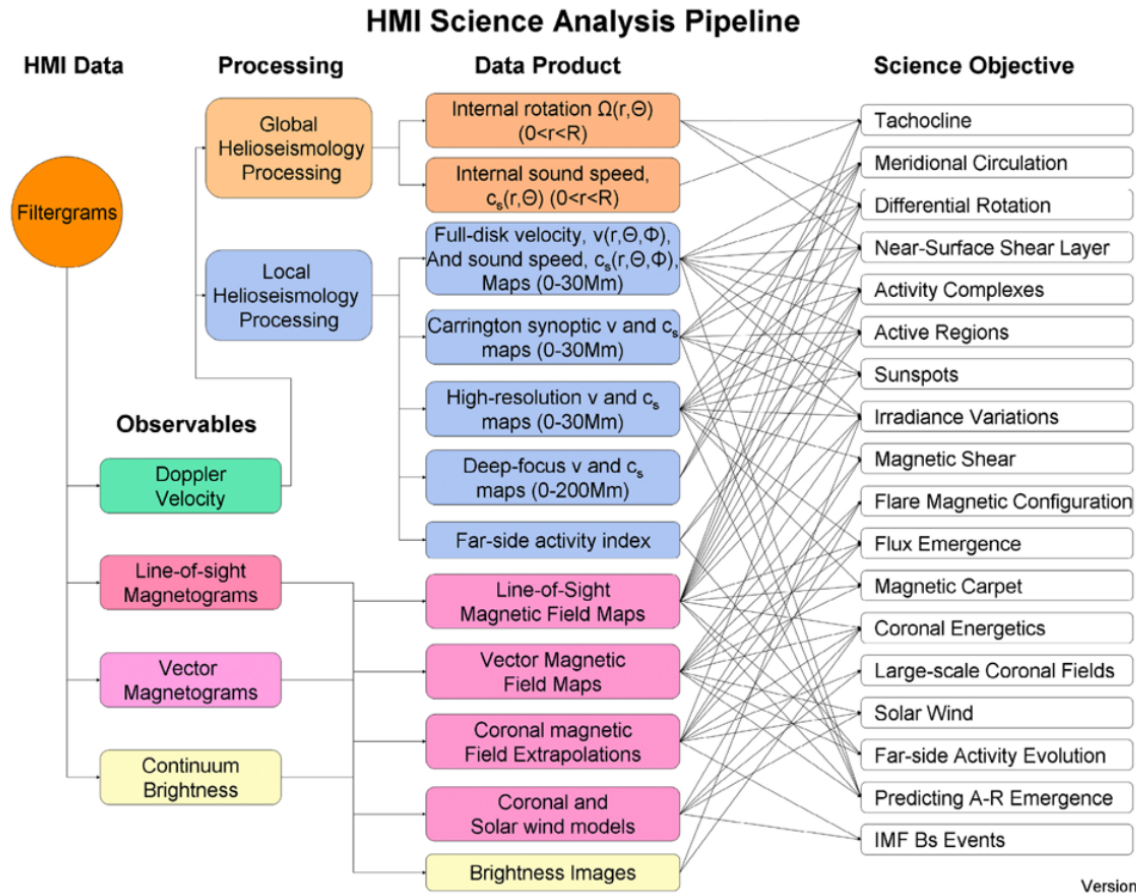
---

[1]HMI Science Plan, pg. 3

Figure 1: Original Figure from Scherrer, J. Schou, et al. (2012) illustrating the HMI Science Analysis Pipeline. Filtergrams are used to produce basic *observables* from which higher level data products are computed. These products inform the science investigations of the science community.

Parameter	Requirement	Performance
Image resolution	<1.5 arcsec	1 arcsec
Doppler velocity image cadence	< 50 sec	45s
Vector magnetic field cadence	< 10 min	90s / 135s (720s)
Data completeness	99.99% image recovery > 95% of the time	Exceeded

Table 1: Original science requirements for HMI. Requirements for errors and precision specific to various data products are listed in their respective CMADs.

resolved measurements of the full vector magnetic field. The quantitative requirements are listed in Table 1. The design of the instrument is described in J. Schou, Scherrer, et al. (2012).

3.2.1 Measurement Concept

The HMI instrument is an imaging spectrograph and polarimeter (see, e.g. Toro Iniesta, J. C. del, 2003), allowing the four Stokes spectra to be measured across the observed absorption line. Line-of-sight velocity is estimated by determining the Doppler shift of the observed line. The vector magnetic field is estimated by performing a Milne-Eddington inversion of the Stokes spectra. Further science data products like line-of-sight magnetic field, continuum intensity images, and spectra line depth and width, are also generated with little additional effort. HMI primarily operates in a synoptic observing mode, interspersed with occasional calibration observations. Special observing campaigns are undertaken very rarely, and usually only during special events (like planetary transits) or spacecraft maneuvers that would preclude the normal science observations.

3.2.2 Instrument Subsystem Description

The HMI instrument consists of a telescope, a set of focus correction optics, a set of polarization selector optics, a set of tunable narrow bandpass filters, and two CCD cameras. Each of these subsystems are described in the following sections.

3.2.2.1 HMI Telescope The HMI telescope is a two element refracting telescope with a 14cm diameter aperture. The first element in the optical path is a 50 Åbandpass filter, which is followed by the primary and secondary lenses. An Image Stabilization System (ISS) using a tip-tilt mirror minimizes image jitter. The HMI calibration and focus-adjustment system allows for coarse focus control using flat plates of varying thicknesses to be placed in the optical path. This system can also place a lens in the optical path which images the aperture. Observations in this latter configuration are frequently referred to as CALMODE, while the normal configuration is referred to as OBSMODE.

Fine focus control is achieved by varying the temperature on the mounting ring of the front window which causes slight changes in its curvature.

3.2.2.2   Polarization Selectors   There are three polarization selectors: two 1/2 waveplates and one 1/4 waveplate. In order along the optical path, their nominal retardances are 10.50, 10.25, and 10.50. They are referred to as PS1, PS2, and PS3, respectively. Each can be rotated through 360° in steps of 1.5°. The polarization selectors are located after the first focus wheel and before the ISS mirror. For normal science observations only two selectors are needed. The third provides redundancy.

3.2.2.3   Tunable Narrowband Filters   The tunable filter system is contained within a precisely temperature controlled oven. The primary components of the filter system are a tunable Lyot filter and two tunable Michelson interferometers. These are preceded in the optical path by a blocking filter. The tunable elements are arranged such that each succeeding component has a narrower free spectral range (FSR); the non-tunable elements arranged in the oposite order. Each tunable element can be tuned to adjust the maximum throughput in wavelength — during normal observations the three are co-tuned to six different target wavelengths across the observing range (twenty wavelength positions are possible). Partial redundancy is provided by an extra movable element between the Michelsons that is not used in normal observations.

3.2.2.4   Cameras   There are two identical cameras fed by a beam splitter. Each camera system consists of a blade-type shutter followed by a 4096×4096 pixel CCD detector with 12.5 micron pixels.

3.2.3   HMI Heritage

3.2.3.1   Instrument Heritage   To a significant extent, the concept and design of HMI is based on the very successful Michelson Doppler Imager (MDI, Scherrer, Bogart, et al., 1995), which was flown on the Solar and Heliospheric Observatory (SoHO) launched in 1996, though HMI is an improvement over MDI in several important respects. Most significantly, HMI can measure all four Stokes parameters and therefore provide full vector magnetic field inversions, whereas MDI only measured circular and one linear polarization states and was limited to line-of-sight magnetic field measurements. Two cameras allow for higher cadence observing as well as greater redundancy in extended mission operations, and the resolution is four times greater in both directions. Finally, the very high data bandwidth afforded by the SDO mission allows for all data taken on board to be downlinked with little onboard processing, allowing for almost continuous coverage in all data products, as well as maximum flexibility on the ground for calibration and if needed re-calibration.
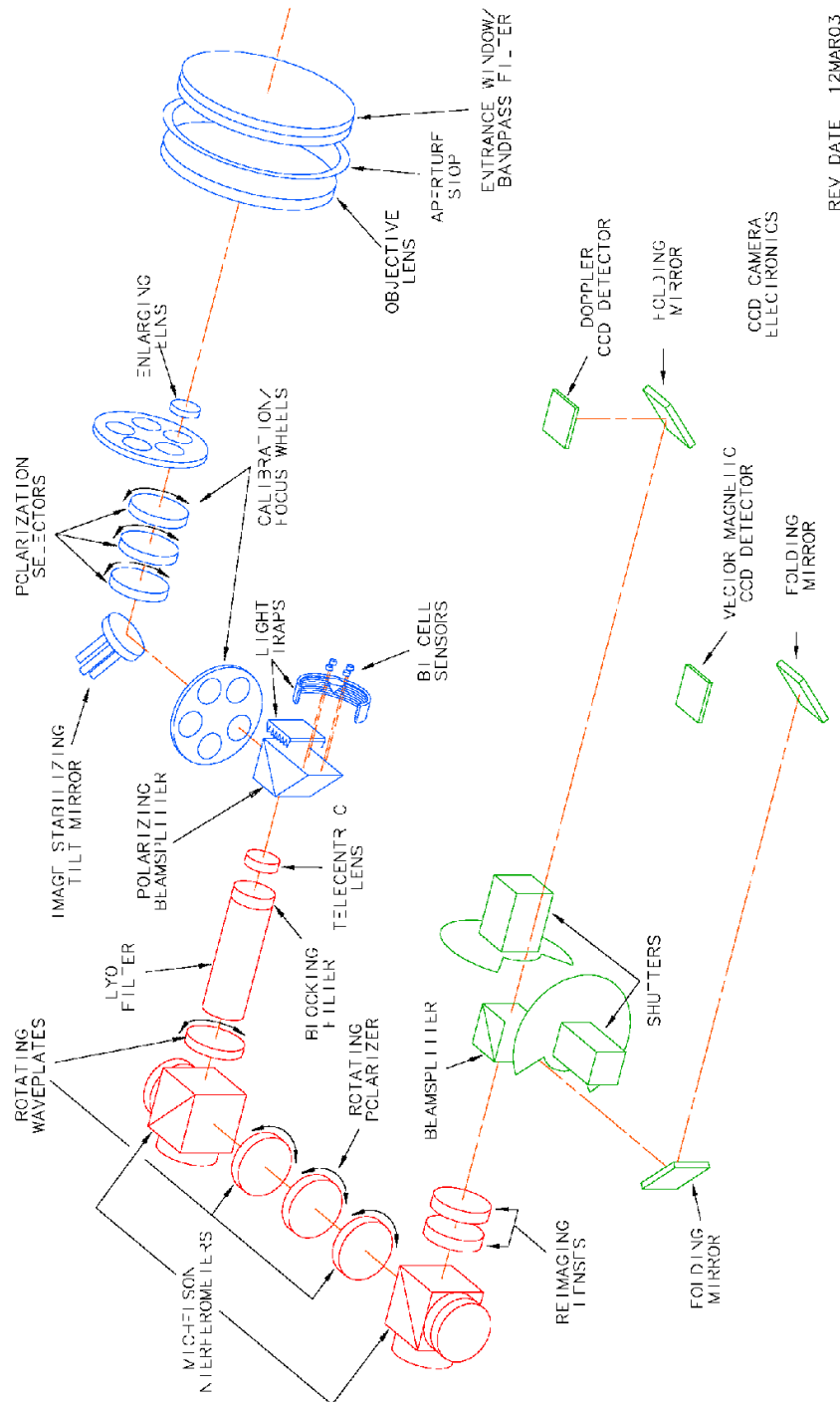
Figure 2: Layout of the optical elements of the HMI instrument. Figure from J. Schou, Scherrer, et al. (2012).
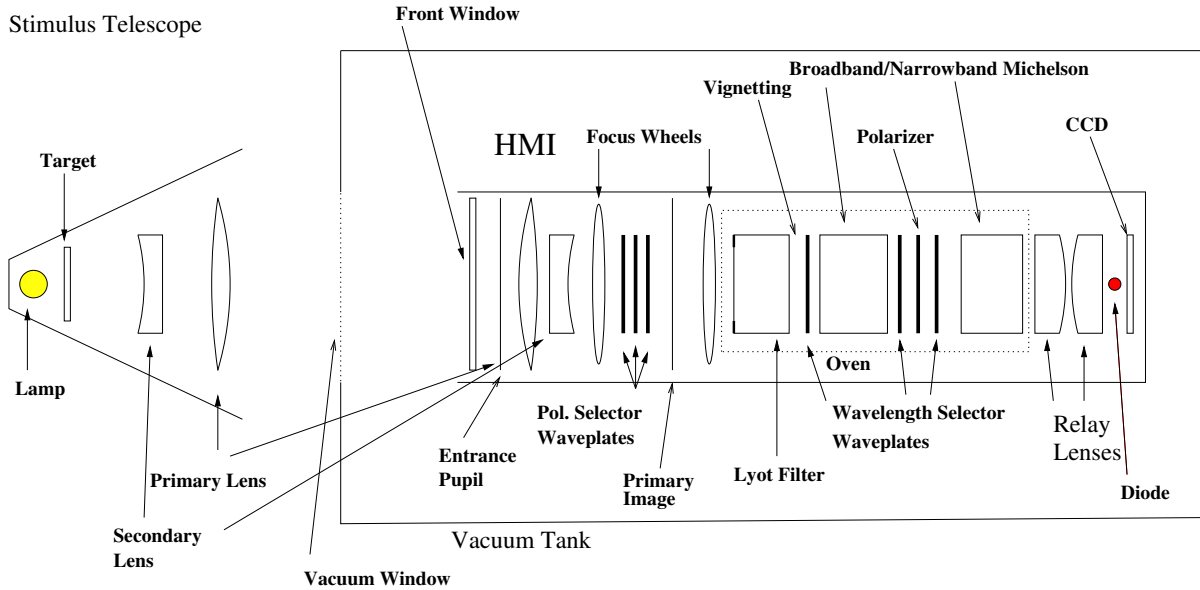
Figure 3: Ground test end-to-end calibration set-ups.

3.2.3.2 Algorithm and Calibration Heritage As the major optical components in the optics package are largely similar to those used in MDI, the calibration schemes used are broadly similar as well, while incorporating lessons learned from the operation of the earlier instrument. The algorithms used to generate calibrated filtergrams and the line-of-sight data products are derived directly from those used for MDI data.

4   HMI Calibration Plan

4.1   Overall Calibration Scheme

Careful measurement of the properties and performance of HMI's various components and subsystems, both during construction and integration and after launch, is critical to producing scientifically useful data and meeting HMI's minimum performance and science requirements. Calibration measurements can be generally split in to pre-launch activities, post-launch activities during the commissioning phase, and finally periodic calibration measurements made during normal operations. In this section, all calibration measurements carried relevant to the optical performance and science data product generation will be discussed.

4.2   Pre-Launch Calibration Overview

Prelaunch calibration measurements include both component tests and end-to-end tests of the integrated flight instrument. Component tests include measurements of transmission and polarization performance of the various optical elements, as well as tests of certain
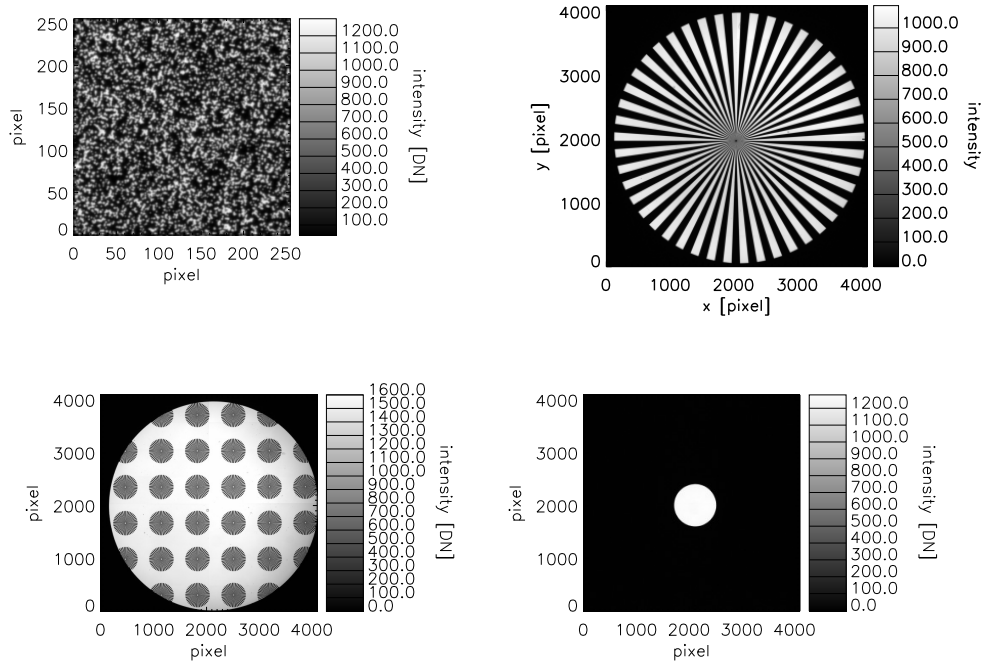
Figure 4: Various targets used in the stimulus telescope. Figure from Wachter et al. (2012).

sub-assemblies, like the Lyot filter. End-to-end tests were performed either in air or in a vacuum chamber. The instrument was illuminated either by a stimulus telescope or by sunlight fed from a heliostat. Schematic representations of the various calibration setups are shown in figure 3. The stimulus telescope consists of an identical optical setup as the flight instrument's telescope, with lenses manufactured to the same standards and specifications as the flight units. The telescope is mounted in the engineering testbed housing. Various targets are placed at the stimulus telescopes focal plane. The most commonly used targets are shown in figure 4.

4.3   On-Orbit Commissioning Overview

After the spacecraft's successful orbit insertion, a period of instrument commissioning and calibration preceded the start or the prime mission. During this period the instrument was prepared for science observations, and some further calibration measurements were taken. In general, these measurements were repeats of some of the calibration activities performed pre-launch, and will not be discussed separately here

4.4   On-Orbit Periodic Calibrations Overview

HMI performs a number of periodic calibration observations at varying cadences. These range from twice-daily measurements run with the normal observing sequence to quarterly calibration observations that involve spacecraft maneuvers. A complete description of these observations can be found in Hoeksema et al. (2018). Some of these measurements are used to monitor instrument trending and guide configuration changes (in particular, focus control, filter tuning, and exposure time). Others are used to calculate and update calibrations applied in the science data processing pipeline. We focus on the latter sets of observations here.

In addition to periodic calibration observations, HMI occasionally performs special calibration observations. Most of these are used for exploratory purposes rather than to directly update calibrations that are currently applied, but planetary transits (two of Mercury, one of Venus) have been used to update the instrument roll angle, as well as verifying the distortion corrections. Temperature variations during lunar transits have precluded using these as roll calibrations.

4.5   Image Quality

Understanding the optical performance of HMI is paramount to providing relevant and accurate science data. This section discusses the various components related to the image quality at the CCDs.

4.5.1   Distortion

There are several ways to measure the distortion of the images. We employ three main procedures for understanding the instrument's distortion: direct measurement, offset images, and on orbit rolls and offsets.

4.5.1.1   Distortion Measurement   To measure the distortion of the images, a random-dot target was used in the stimulus telescope setup. With various alignments in the leg positions, the team took images of specific 256×256 pixel section of the target at different optical field positions and cross-correlated them. This provides the differences in the leg positions and the amount of distortion in the region, as a function of field positions expanded in Zernike polynomials, see equation (1).

$$Z_n^m(\rho, \phi) = \begin{cases} N_n^m R_n^m(\rho) \cos m\phi & \text{if } m \geq 0 \\ -N_n^m R_n^m(\rho) \sin m\phi & \text{if } m < 0, \end{cases} \tag{1}$$

where ϕ is the azimuthal angle and ρ is the normalized radial distance ($o \leq \rho \leq 1$).

Following the plan discussed in document HMI-S020, the team fitted the coefficients, $a(n, m)$, of a 23rd order Zernike polynomial, given by the expression

$$D^f(\rho, \phi) = \sum_{n=2}^{23} \sum_{m=-n}^{n} a(n, m) Z_n^m \tag{2}$$

These distortion measurements were taken from June 2007 to August 2009 for each of 29 sets (Wachter et al., 2012). Results from the measurements can also be seen in the aforementioned reference. Fit coefficients are stored as plain text files that are read by the software routines discussed in 5.2.2.2. The distortion maps are shown in Figure 5.

4.5.2   Image Scale

As mentioned in 4.5.1, the ellipticity, image scale, and roll angle are determined on-orbit. This is done by looking at the size of the solar disk (see §5.4 of Wachter et al. (2012)). The roll calibration was performed twice during the Venus and Mercury transits that happened in 2012 and 2016, respectively. The image scale is determined for each filtergram in normal science mode observations (see section 5.2.2.1). The roll angles used were updated after the Venus transit. The currently used values for the orientation of each camera with respect to the spacecraft orientation are 180.013504° and 179.929794° for cameras 1 and 2, respectively.
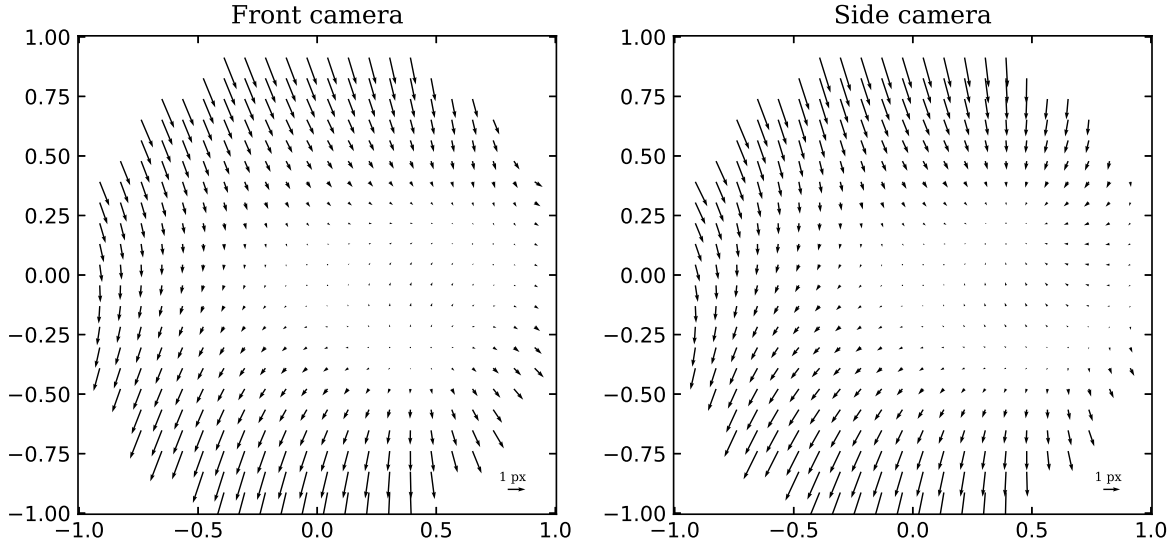
Figure 5: Distortion maps for both cameras.

4.5.3   Focus and Co-alignment

Determining the pre-flight best focus was measured using a random-dot target during a focus sweep by observing the maximum spatial power at intermediate frequencies. A quadratic function was fit to the average power as a function of the focus position. More details of this procedure can be found in (Wachter et al., 2012).

Alignment of the cameras was determined from simultaneous focus sweeps on both cameras using cross-correlation techniques. A relative lateral shift and rotation for the images of the two cameras was derived and determined to have a slight lateral shift drift over the time scale of several months. The shifts are very accurately measured in space and monitored continuously.

4.5.4   Modulation Transfer Function (MTF)

The Modulation Transfer Function (MTF) was measured through direct and relative methods, similar to the distortion section. We also perform some on-orbit measurements throughout the mission lifetime. The following section describes the procedures for measuring the MTF.

4.5.4.1   MTF Measurement   Direct measurements of the square-wave MTF were performed using the stimulus telescope with the Ronchi and star targets. The star target

was remapped to polar coordinates and a sine wave was fitted for each radial distance. The amplitude of the spatial frequency via pixel integration is given by equation (3).

$$A(\lambda) = \text{MTF}(\xi) \frac{4 \sin \pi \xi}{N \pi \xi} \left| \sum_{n=0}^{N/s-1} \frac{2}{1 - \exp 2\pi i \xi} \right| \tag{3}$$

where ξ is the spatial frequency, N is the pixel dimension of the CCDs, and $s = 1/\xi$ is the wavelength.

The MTF can also be derived from images of the random-dot target by removing the power spectrum of the target, given by equation (4).

$$\text{MTF}(\lambda) = \frac{\int p(\xi, \phi) d\phi}{\int t(\xi, \phi) d\phi}, \tag{4}$$

where $p(\xi, \phi)$ is the power spectrum of the image, and $t(\xi, \phi)$ is the power spectrum of the target, both in polar coordinates.

The team also determined the MTF of the instrument itself in order to understand whether the two camera images could be combined. This was done by performing focus sweeps of the random-dot target for the stimulus telescope and the perfect instrument. The results provided a difference between the two as a function of spatial and focus positions. The data are the same or similar to what was used for the distortion focus.

4.5.5   Scattered Light

The team determined the need to develop a point spread function (PSF) for the instrument. A Lorentzian convolved with an Airy function is used as our PSF. The ideal form of the PSF is proportional to the Bessel $J1$ for non-negative intensity and is given in equation (5)

$$\text{PSF}_{\text{ideal}}(r) = \left(\frac{2 J_1(r')}{r'} \right)^2 \ni r' = \frac{\pi D r}{f \lambda}, \tag{5}$$

where r' is a normalized radius, D is the diameter of the telescope aperture (14cm), f is the effective focal length (4953mm), and $\lambda = 6173\text{Å}$.

The PSF was determined based on three sets of observational data, a set of pre-launch data, data during the 2012 Venus transit, and a set of data from lunar occultation. Pre-launch observations used the star target during ground calibrations to determine the MTF. During the Venus transit, we used both simulation and observational data to determine local scattering. While the lunar occultation data was used to determine global scale scattering.

During the planning phase of the mission, an empirical model with 4 parameters developed by Pierce and Slaughter (1977) was used as our PSF; given by equation (6).

$$A(r) = (1 - \epsilon)e^{-(r/w)^2} + \frac{\epsilon}{1 + (r/W)^\kappa}, \tag{6}$$

where r is the radial distance, ϵ determines the relative sizes of the two parts, w is the $1/e$ width of the central Gaussian core, W is the half-width at half-maximum width of the extended tail, and κ determines how fast the extended tail drops off. The best fit parameters were determined to be $\epsilon = 0.1$, $\kappa = 3.0$, $w = 1.8$, and $W = 3.0$ (Wachter et al., 2012).

For the June 6th, 2012 Venus transit, true continuum images were used to determine local scattering. The least amount of fluctuations in the disk intensity occurred between 02:04-02:46 UTC and were therefore used for the analysis. For the analysis, Venus was assumed to be a perfect sphere and filtergrams used had only spacial distortion removed. There is likely no unique solution when solving for the PSF, so forward modeling was performed on simulated continuum data as well.

As several lunar eclipses occur throughout a year, the October 7th, 2010 date was picked for the global scattering PSF analysis. Similar steps were taken to perform forward modeling on simulated data with Moon ephemeris data. Distances of 10", 100", and 700" off the solar disk were analysed for the global scattering contributions.

Once a PSF was determined, deconvolution is done of the data using an iterative Richardson-Lucy algorithm (Richardson, 1972; Lucy, 1974). For the 45 second data, this deconvolution is performed to each filtergram after flat-fielding, dark current, and distortion corrections are applied, but before the filtergrams are combined to create the definitive images. However, for the 720 second Stokes data, this deconvolution is applied at the end of the definitive processing steps. Although some data are currently available for use today, the data is generally created only on request. All deconvolved, or PSF corrected, data products are given the same series name with the suffix "_dcon" or "_dconS", for 45 second and 720 second products, respectively.

4.6   CCD and Camera

Calibration of the CCDs and cameras is largely accomplished with on-orbit observations.

4.6.1   Bad Pixels

A small number of bad pixels (none in camera 1, three in camera 2) are permanently bad. In addition, pixels in the offpoint flatfields (see 4.6.3) having less than 50% of the average gain are flagged as permanently bad.

4.6.2   Dark Current

The CCD bias, or pedestal and dark current, is determined from zero-exposure camera readouts performed during the flatfield offpoints. Several dark frames are averaged together. Daily dark frames are taken for performance monitoring but are not used in image calibration.

4.6.3   Flat Field

Accurate dermination of the pixel-to-pixel variation in gain is critical for producing science-quality filtergrams and all subsequent science data products. The array of gain coeffients $F(\mathbf{x})$ is referred to as a flatfield, where $\mathbf{x}$ is the position on the detector in pixel coordinates. Flatfields are computed separately for each camera, and follow the technique described in Kuhn, Lin, and Loranz (1991). Assuming the bias level as already been removed, the measured image pixels $I(\mathbf{x})$ relate to the source signal $S(\mathbf{x})$ by

$$I(\mathbf{x}) = F(\mathbf{x}) \cdot S(\mathbf{x}). \tag{7}$$

If the source $S(\mathbf{x})$ is invariant over a series of subsequent observations, offsetting the images by some distance $\mathbf{a}$ can be used to solve for $F(\mathbf{x})$. The derivation of the algorithm used here can be found in Kuhn, Lin, and Loranz (1991).

   The flatfield is updated for each camera weekly. Offpointed solar images are obtained in two ways. Weekly calibration observations use the ISS to offset the solar image by a few pixels in various directions. This is repeated twenty four hours later to allow solar features to rotate to a different part of the image and minimize systematic errors caused by solar activity. For larger scale offsets, the entire spacecraft is moved. These flatfield offpoint maneuvers are performed four times per year. Flatfields are computed separately for the maneuver offpoint and ISS offset calibration data and then combined to produce the flatfield used in data calibration. The former flatfield is referred to as the offpoint flatfield. The latter is referred to as the PZT flatfield, which refers to the PZT actuators on the ISS mirror that are used to drive the mirror for the image offsets. The algorithm used to generate both the offpoint flats and the PZT flats is the same, but the image selection and preparation are done differently.

4.6.3.1   Image apodization   Throughout the flatfield determination, filtergrams are circularly apodized at various stages to eliminated systematic errors from the edges of the images or areas off the solar limb. While the parameters chosen vary, the apodization function used is

$$
w(r) = \begin{cases} 1 & \text{if } r \leq r_{\text{in}} \\ \cos\left(\pi \frac{r - r_{\text{in}}}{r_{\text{out}}}\right) & \text{if } r_{\text{in}} < r < r_{\text{out}} \\ 0 & \text{if } r \geq r_{\text{out}} \end{cases} \tag{8}
$$

where $r = |\mathbf{x} - \mathbf{x}_{\text{cen}}|$.

4.6.3.2   Offpoint flatfield filtergram preparation   SDO performs a series of off-point maneuvers every three months, with approximately 45 dwell periods at offsets from Sun-centered pointing of up to 600 arc seconds. Dwell times vary between six and ten minutes, which includes the slew and settling times for the spacecraft. In all, the maneuvers take approximately six hours to complete, and are used by all three SDO instruments for calibration purposes. The offpoint pattern is shown in Figure 6. During these maneuvers, both cameras on HMI take a series of filtergrams at fixed polarization and wavelength but various focus settings, as well as dark frames. For the determining the flatfield, only filtergrams with the current focus setting are used. Filtergrams are then grouped into different pointings (defined by pointing variation frame-to-frame of less than 3 arc seconds). Filtergrams whose pointings deviate by more than 2 arc seconds from the mean are rejected. A reference set of filtergrams, with Sun-centered pointing, are selected, and offsets $\mathbf{a}_i$ are determined by maximizing the covariance

$$
|I_i(\mathbf{x} + \mathbf{a}_i) * I_0(\mathbf{x})|. \tag{9}
$$

The same algorithm is used to determine the center coordinates of the solar disk in each image by shifting each image against itself rotated 180°.

Once the filtergrams have been selected, grouped, and the image coordinates have been determined, the images are prepared. The dark current is subtracted from each filtergram (see section 4.6.2). For each offpoint position the filtergrams are averaged to a single image, with pixels that exceed the median at that image position by more than 1500 are rejected. Active regions and plage regions must be masked out. The solar image is flattened by removing a fifth order polynomial in $\mu = \sqrt{1 - r_{\text{sun}}^2}$, where r_{sun} is the fractional distance from the center of the solar disk, and pixels that deviate more than 15% from the average level are masked. The coeffients in the limb darkening polynomial are (0.229947, 1.99002,-4.01991, 5.96688, -4.53731, 1.37037). An example of prepared filtergrams is shown in Figure 7

4.6.3.3   PZT flatfield filtergram preparation   HMI performs a set of small-displacement flatfield calibration obervations every week, using the Image Stabilization System mirror to offset the solar image by up to 20 arc seconds. The observations are taken both at
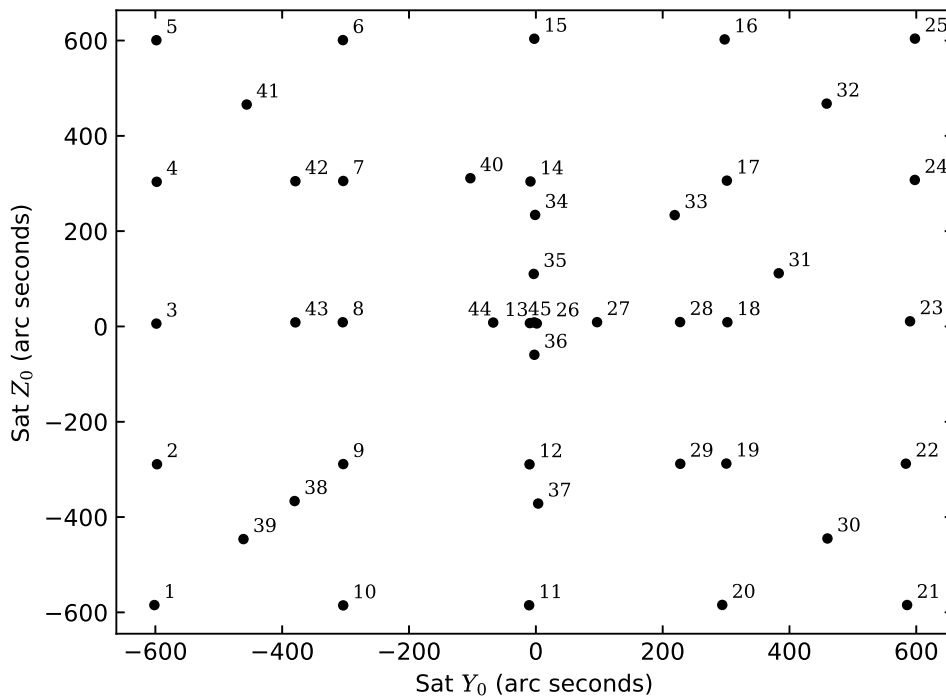
Figure 6: Typical offpoint positions for flatfield offpoint maneuvers. This example is the actual offpoint positions used for the 2022 October 5 flatfield offpoints. The points are numbered with the order they were taken in.
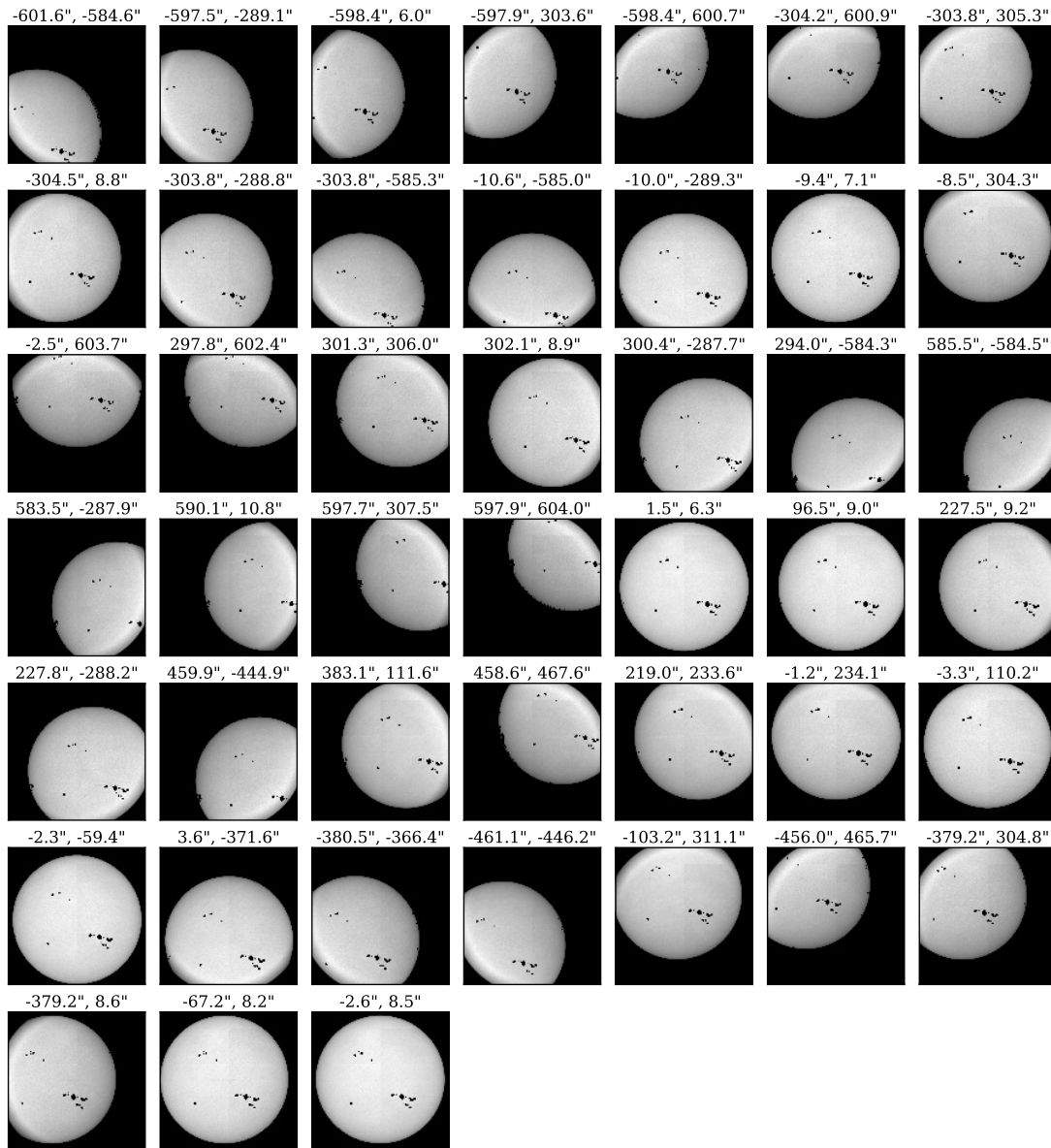
Figure 7: An example of averaged and masked filtergrams from the 2022 October 5 offpoint maneuvers. The data are from camera 1. The offsets for each poiting in arc seconds are shown above each image. Active regions and plage regions have been masked and set to an invalid value so they will not contribute to the flatfield determination.

the default focus setting and in CALMODE, although only the standard focus setting filtergrams are used to calculate the flatfields. A fixed set of eleven offpoint positions is repeated approximately twenty four hours apart to allow solar active regions to rotate to a different part of the solar disk. A single filtergram is taken at each position each day. Because the entire solar limb remains within the instrument's field of view the standard image coordinates can be used for solar radius and center position.

Outlier detection is done in the same as with the offpoint flatfield filtergrams, but pixels are simply masked rather than replaced. Active region masking is also done in the same way. The PZT flatfield is determined twice, once for each day's observations.

4.6.3.4 Flatfield determination The determination of the flatfield correction follows the method of Kuhn, Lin, and Loranz (1991). For a given set of images $I_i(\mathbf{x}_i)$ with offsets $\mathbf{x}_i = \mathbf{x}_0 + \mathbf{a}_i$, a flatfield is determined by iterating from the initial solution $G_0(\mathbf{x}) = \log(F_0(\mathbf{x})) = 0$. The solution at $r + 1$ is given in terms of $G_r(\mathbf{x})$ by

$$G_{r+1}(\mathbf{x}) = K(\mathbf{x}) + \frac{1}{w(\mathbf{x})} \sum_{i<j} \left[G_r(\mathbf{x} - \mathbf{a}_i + \mathbf{a}_j) + G_r(\mathbf{x} - \mathbf{a}_j + \mathbf{a}_i) \right], \tag{10}$$

where

$$K(\mathbf{x}) = \frac{1}{w(\mathbf{x})} \sum_{i<j} \left[\log I_i(\mathbf{x}) - \log I_j(\mathbf{x} - \mathbf{a}_i + \mathbf{a}_j) + \log I_j(\mathbf{x}) - \log I_i(\mathbf{x} - \mathbf{a}_j + \mathbf{a}_i) \right]. \tag{11}$$

The weighting function $w(\mathbf{x})$ is the sum given by

$$w(\mathbf{x}) = \sum_{i<j} n(\mathbf{x}) \cdot w_{\text{image}}(\mathbf{x}) \cdot w_{\text{sun}}(\mathbf{x}). \tag{12}$$

The function $n(\mathbf{x})$ is 1 where $\mathbf{x}$ is a valid pixel (not off the edge of detector) and the pixel value is greater than zero (i.e., not masked solar activity), and 0 otherwise. The functions $w_{\text{image}}(\mathbf{x})$ and $w_{\text{sun}}(\mathbf{x})$ are apodization functions given by equation (8). The former is centered on the image, the latter is centered on the solar disk. Thus, equation (12) ensures that only valid pixels are counted in the sum (10) and the contribution decreases smoothly towards the edge of each image and off edge of the solar disk.

4.6.3.5 Combination The two PZT flatfields are averaged together, with only pixels with valid solutions used. The averaged PZT flatfield is them multiplied by the most recent offpoint flatfield, and normalized. The normalization scaling is the average of the pixel gains within 1970 pixels of the image center. An example of offpoint and combined flatfields is show in Figure 8.

Camera 1   Camera 2
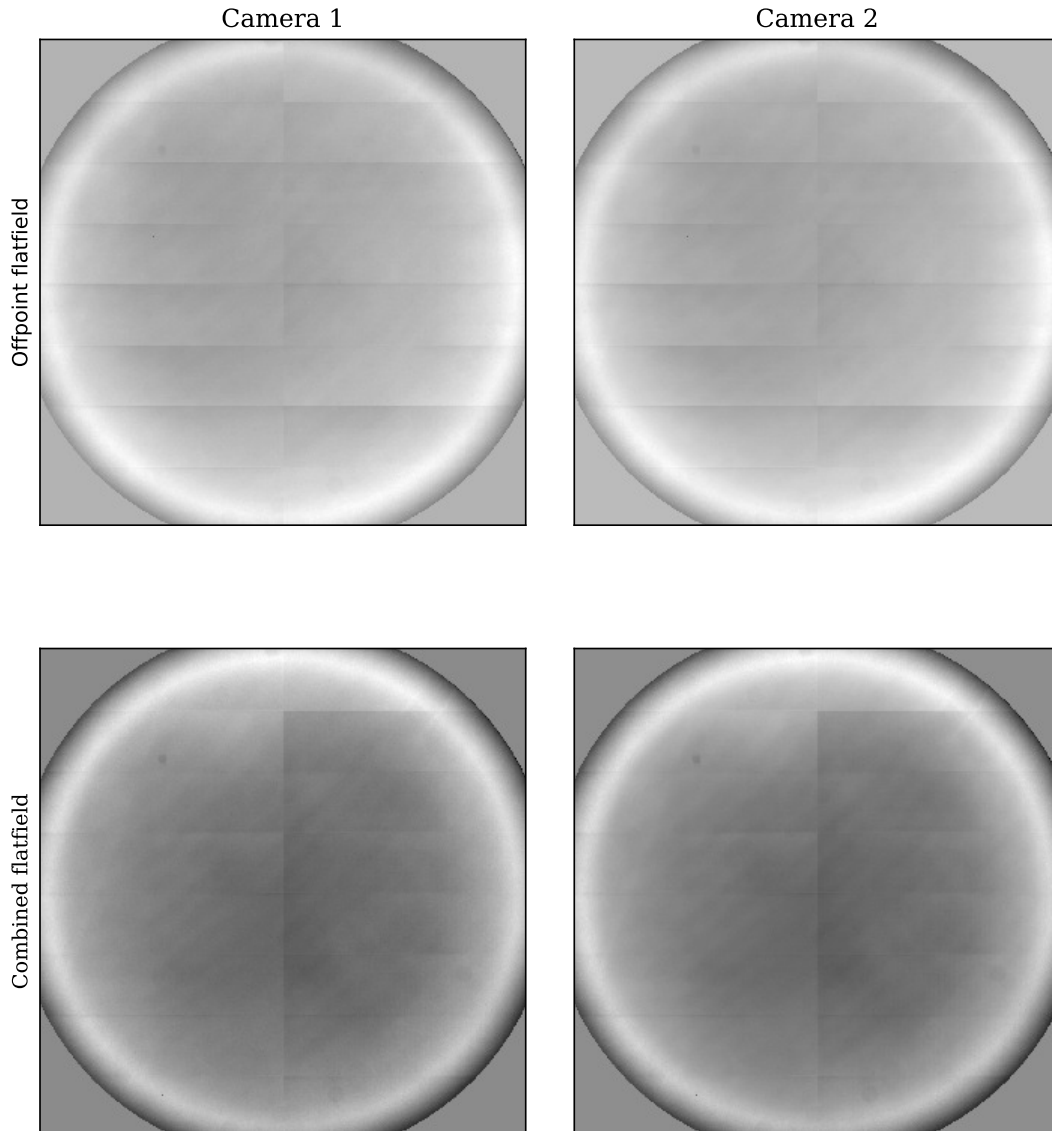
Figure 8: Examples of offpoint and combined flatfields for both cameras. The offpoint flatfields (top row) are computed from the offpoint maneuvers on 2022 Oct 5. The combined flatfields (bottom row) use the offpoint flatfields from 2022 Oct 5 and PZT flatfield observations from 2022 Oct 11 & 12. These combined flatfields were used to correct level 1 filtergrams between 2022 Oct 11 19:15:42 TAI and 2022 Oct 18 19:03:41 TAI. The rectangular patterns are residuals from the fabrication of the CCDs.

Before 2014.01.15 (CALVER bit 0x1000)				
Camera 1	-8.2799134	0.017660396	-3.7157499e-06	9.0137137e-11
Camera 2	-11.081771	0.017383740	-2.7165221e-06	6.9233459e-11
After 2014.01.15 (CALVER64 bit 0x2000)				
Camera 1	0.0	0.025409177	-4.0088672e-06	1.0615198e-10
Camera 2	0.0	0.020677687	-3.1873243e-06	8.7536678e-11

Table 2: Third order polynomial coefficients for the CCD non-linearity correction. The CALVER32 and CALVER64 keywords describe which calibration was used if any, see Appendix E.3.

4.6.4   CCD Non-Linearity

Determination of the non-linearity of each CCD is accomplished using a sequence of exposures of increasing length. A third-order polynomial is fit to the entire field-of-view. Prior to 2014 January 15, the linearity correction coefficients were based on data taken during ground calibration on 2008 July 23 (Wachter et al., 2012). After 2014 January 15, the coefficients used are a mean of several on-orbit observations. The coefficients used are given in Table 4.6.4.

4.7   Image Motion

During the on-ground calibration phase, the team looked at how various moving components, such as the 6 rotating waveplates and one rotating polarizer, affect image offset. Relative image shift was determined by cross-correlating each image with the random dot reference image. It was determined that the second and fourth wavelength selector waveplates had the most significant contribution to image motion with approximately half a pixel vertical shift. As the image center and plate scale is measured for every filtergram used in science data processing, these shifts are taken into account along with other sources of image motion.
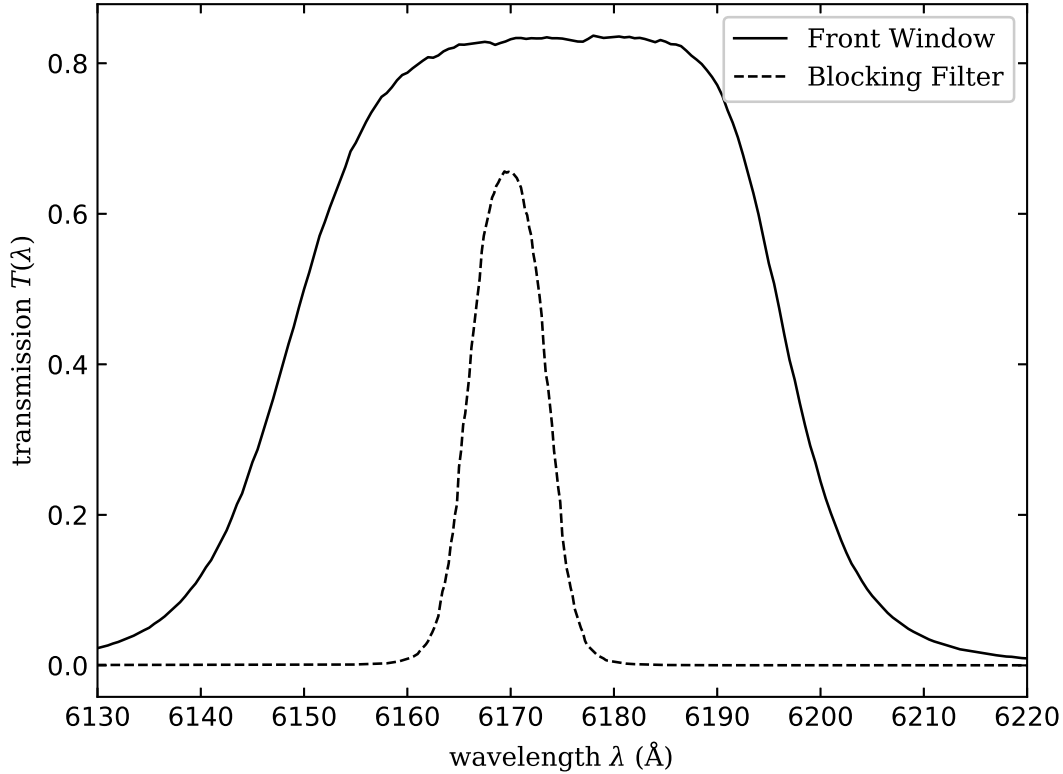
Figure 9: Spatially-averaged transmission profile of the blocking filter (dashed line) and front window (solid line).

4.8 Wavelength Calibration

The optical filter system of the HMI instrument consists of a front window, a blocking filter, a five-stage Lyot filter, and two Michelson interferometers. For a complete discussion of the design choices and performance characteristics see Sébastien Couvidat, Jesper Schou, et al. (2012). Calibrating the wavelength performance consists primarily of measuring the wavelength-dependent properties of each element of the filter system (primarily a pre-launch activity), determining the optimal positions, or tunings, of each moveable optical element to achieve the desired transmission, and measuring the actual transmission performance across the field (performed regularly on-orbit).

4.8.1 Wavelength Dependence

Determination of the instrument transmission as a function of wavelength is discussed in detail in Sébastien Couvidat, Rajaguru, et al. (2012) and further in S. Couvidat et

al. (2016). This transmission profile can be calculated as the product of the individual optical elements: the front window $T_{\text{FW}}(\lambda)$, the blocking filter $T_{\text{BF}}(\lambda)$, the Lyot filter $T_{\text{L}}(\lambda, \phi_{\text{L}})$, and the two Michelson interferometers $T_{\text{NB}}(\lambda, \phi_{\text{NB}})$ and $T_{\text{WB}}(\lambda, \phi_{\text{WB}})$, where ϕ is the selected phase of each tunable element. The transmission profiles of the blocking filter and front window were determined during pre-launch calibrations, and are assumed not to have changed. The transmission of each Michelson interferometer is modeled as

$$T(\lambda, \phi)_i = \frac{1 + B_i \cos(2\pi\lambda/\text{FSR}_i + \Phi_i + 4\phi_i)}{2} \tag{13}$$

where B_i is the contrast and Φ is the relative phase. The free spectral range (FSR) is assumed not to vary with time. The lyot filter consists of five individual elements E1 through E5. Elements E2 through E5 are not tunable, and are modeled as

$$T(\lambda)_{\text{E}i} = \frac{1 + B_{\text{E}i} \cos(2\pi\lambda/\text{FSR}_{\text{E}i} + \Phi_{\text{E}i})}{2} \tag{14}$$

while the transmission of E1 is given by the same equation as the Michelsons in equation 13. The total transmission of the instrument as a function of wavelength is therefore

$$T_{\text{HMI}}(\lambda) = T_{\text{FW}}(\lambda) \times T_{\text{BF}}(\lambda) \times T_{\text{L}}(\lambda, \phi_{\text{E1}}) \times T_{\text{WBM}}(\lambda, \phi_{\text{WBM}}) \times T_{\text{NBM}}(\lambda, \phi_{\text{NBM}}). \tag{15}$$

Thus, calibration of the filter section of the HMI instrument requires determining the phases, contrasts, and free spectra ranges for the three tunable elements and four non-tunable elements, as well as the transmission profile of the front window and blocking filter as a function of wavelength.

4.8.2   Phasemaps

The intensity I_{HMI} measured by HMI's cameras is the intensity I that enters the instrument convolved with the instrument transmission profile T_{HMI}:

$$I_{\text{HMI}} = \int I(\lambda) \cdot T(\lambda, \phi_{\text{E1}}, \phi_{\text{WBM}}, \phi_{\text{NBM}}) d\lambda. \tag{16}$$

If I is sufficiently well known, measurements of I_{HMI} with different settings of the wavelength selectors ϕ_i can be used to solve for the unknowns in the transmission profile — that is, the phases Φ_i. In the case where I is sufficiently close to truly monochromatic at wavelength λ_0, as in the light from a laser source, this becomes

$$I_{\text{HMI}} = I \cdot T(\lambda_0, \phi_{\text{E1}}, \phi_{\text{WBM}}, \phi_{\text{NBM}}), \tag{17}$$

which allows the unknown parameters to be solved for easily. When the observed light source is not so simple, as in the Sun, solving for the phases Φ_i is somewhat more difficult.

For solar observations, we treat the solar intensity as a flat continuum with the FeI absorption line subtracted from it. The absorption line is modeled as a Voigt profile
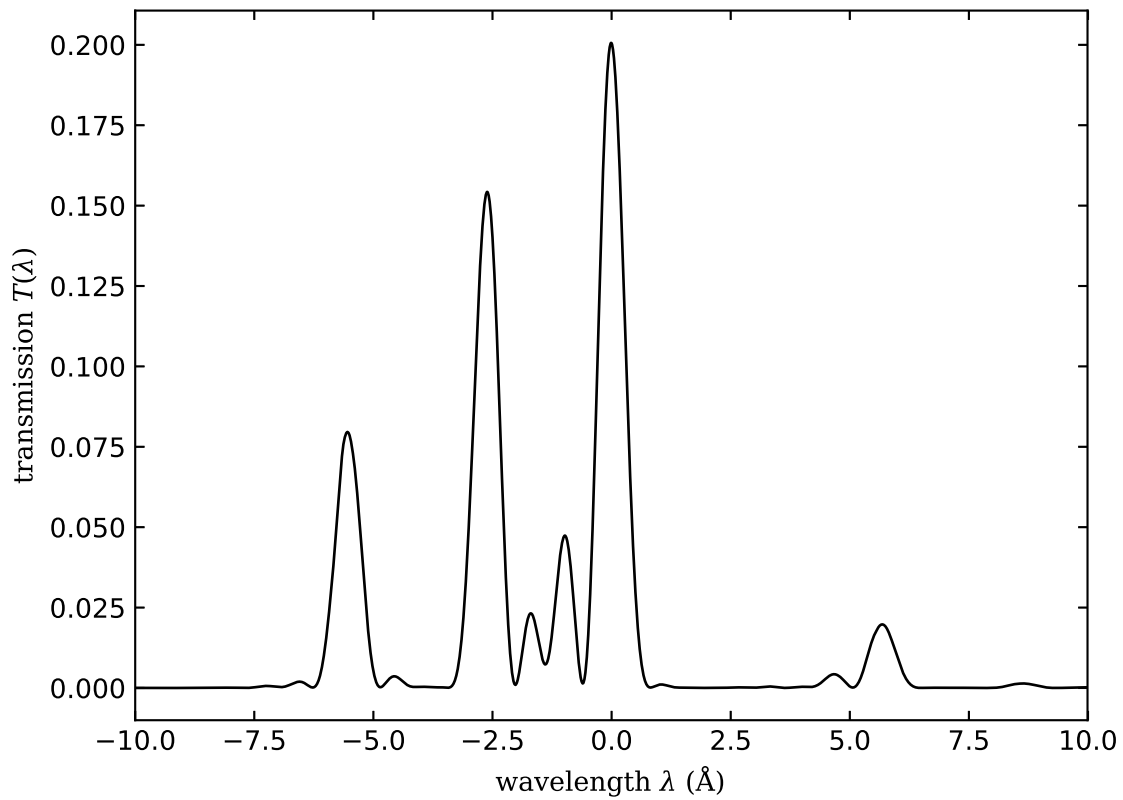
Figure 10: Transmission profile for the non-tunable elements in the filter section (E2 through E5 in the Lyot filter) and the front window and blocker. The profile is averaged through the center of the field.

Cal	I_g	d_g	w_g	A	B	C	D	E	F	a
11	1.0	0.5625	0.06415	0.015	0.225	0.2	0.004	0.15	0.22	0.03
12	1.0	0.53	0.0615	-0.01	0.225	0.02	0.015	0.10	0.25	0.03
13	1.0	0.58	0.058	-0.0074	0.2	0.13	0.012	0.05	0.18	-0.09

Table 3: Parameters for synthetic FeI absorption (equation 18). Different values of these parameters have been used as the instrument calibration has been updated. Calibration 11 was used until 2012 January 18, then calibration 12 was used until 2014 January 15, and calibration 13 has been used since.

(Tepper-García, 2006) and two Gaussian profiles. The Gaussians are added to match the asymmetry in the actual solar absorption line. The line profile is given by:

$$I_{\text{FeI}}(\lambda) = I_g - d_g \exp\left(-l^2\right)\left(1 - \frac{a}{\sqrt{\pi}l^2}\left[(4l^2+3)(l^2+1)\exp(-l^2) - \frac{2l^2+3}{l^2}\sinh(l^2)\right]\right)$$
$$- A\exp\left(-(\lambda+B)^2/C^2\right)$$
$$+ D\exp\left(-(\lambda-E)^2/F^2\right), \quad (18)$$

where $l = \lambda/w_g$ and $|l| \leq 26.5$, and

$$I_{\text{FeI}}(\lambda) = I_g - A\exp\left(-(\lambda+B)^2/C^2\right) + D\exp\left(-(\lambda-E)^2/F^2\right) \quad (19)$$

otherwise. The parameters used are given in table 3. The parameter w_g controls the width of the Voigt profile, and d_g is the line depth.

For a given set of N observations $\text{I} = [I_0, \ldots, I_{N-1}]$ with varying wavelength selector positions, the sum

$$S(\Phi_{\text{E1}}, \Phi_{\text{WBM}}, \Phi_{\text{NBM}}, w_g, d_g) = \sum_{j=0}^{N-1}\left(\int I_{\text{FeI}}(\lambda)T_{\text{HMI}}(\lambda, \phi_{\text{L},j}, \phi_{\text{WB},j}, \phi_{\text{NB},j})d\lambda - I_j\right)^2 \quad (20)$$

can be minimized over $\Phi_{\text{E1}}, \Phi_{\text{WBM}}, \Phi_{\text{NBM}}$. The solar line itself varies, however, so the line depth d_g and width w_g also need to be allowed to vary. Note that varying the width parameter only affects the Voigt profile width and does not affect the contribution from the Gaussians. The wavelength λ is relative to $\lambda_0 + \langle v_{\text{obs}}\rangle d\lambda/dv$, where $\lambda_0 = 6173.3433$ Åis the rest wavelength of the center of the FeI line and $\langle v_{\text{obs}}\rangle$ is the average of the line-of-sight velocity of the spacecraft with respect to the Sun over the detune sequence. To generate phasemaps from a given set of observations (see section 4.8.4), the Jacobian of S is constructed by calculating the derivatives of S with respect to the five fit parameters by finite difference. The least squares problem is solved with the use of a singular value decomposition. For the purposes of monitoring the ongoing instrument performance, and choosing when to retune, averages of the three phases are made. The averaging area is a circle with a radius of approximately 56 pixels at the center of each phasemap.

Element	Nominal FSR	Measured FSR	Current FSR
NB	172	172	168.9
WB	344	343.1	336.85
E1	690	693	695
E2	1380	1407	1417
E3	2758	2779	2779
E4	5516	5682	5682
E5	11 032	11 354	11 354

Table 4: Free spectral ranges (FSRs) of the three tunable and four non-tunable elements in the filter section, given in mÅ. The nominal FSRs are the design specifications, the measured FSRs are those determined on the ground, and the current FSRs are those currently used in instrument calibration and data processing.

4.8.3   Ground Calibration

The ground calibration of the HMI filter system was performed throughout the pre-launch period, and is described in full in Sébastien Couvidat, Jesper Schou, et al. (2012). While all phases, contrasts, FSRs, and trasmission profiles were measured throughout the ground calibration phase, we focus here on the parameters that have not been re-determined on orbit: the transmission profile of the front window and blocking filter, the phases and contrasts of the non-tunable elements, and the contrasts of the tunable elements. The transmission of the front window and blocking filter is shown as a function of wavelength in Figure 9. Only the average across the field is known.

The free spectral ranges of the seven optical elements were measured either by the element manufacturers or during instrument assembly. They are shown in Table 4.

The phases and contrasts of the non-tunable elements were determined during ground calibrations using a variety of test-setups and observing sequences. A tunable dye laser was used to take many observations at different wavelengths and instrument configurations (see Sébastien Couvidat, Jesper Schou, et al., 2012, for a full discussion) so that the contrasts and phases of the non-tunable elements could be fit.

With a light source with a sufficiently narrow wavelength range, the phases and contrasts of the tunable elements can be determined analytically with a sequence of observations with different filter settings. The transmission profile for the non-tunable section is shown in Figure 10.

4.8.4   On-Orbit Calibration

While some parameters cannot reliably be measured on orbit (the contrasts and transmission profiles, in particular), some others are better determined on orbit, either because the ground calibration setup does not adequately match the environment in space or because these parameters vary with time. This latter is particularly relevant for the phases of the tunable elements, which drift with time, and so maps of the element phases are
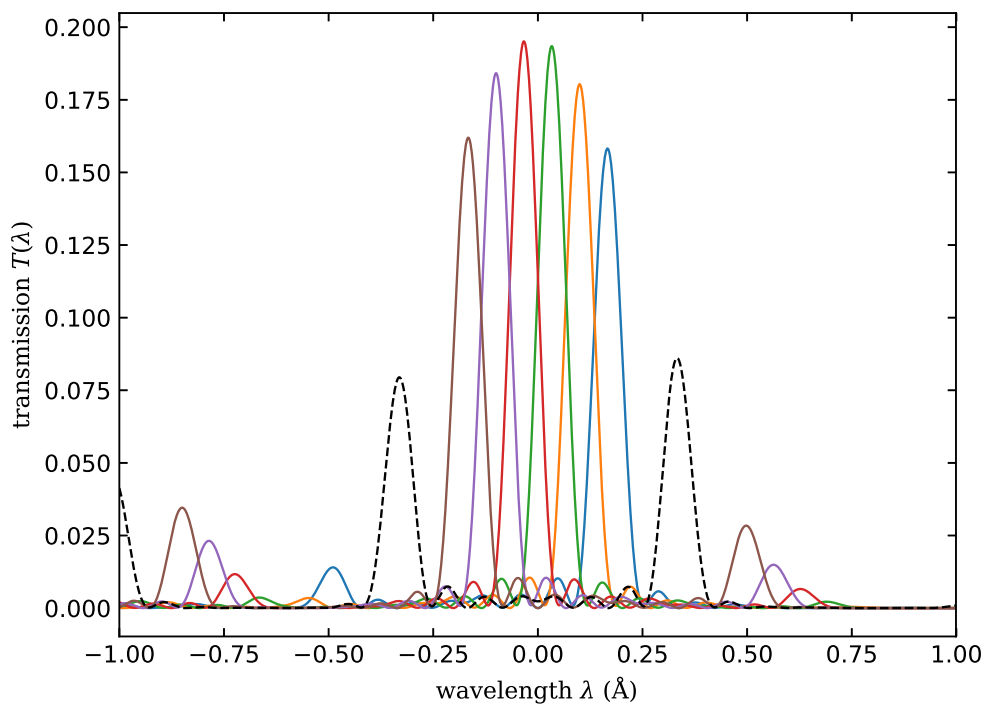
Figure 11: An example the HMI filter transmission at the six different tuning settings used in normal operations (shown as solid lines in color). The continuum tuning is also shown (dashed line) which has sensitivity on either side of the absorption line when the relative velocity is close to zero.
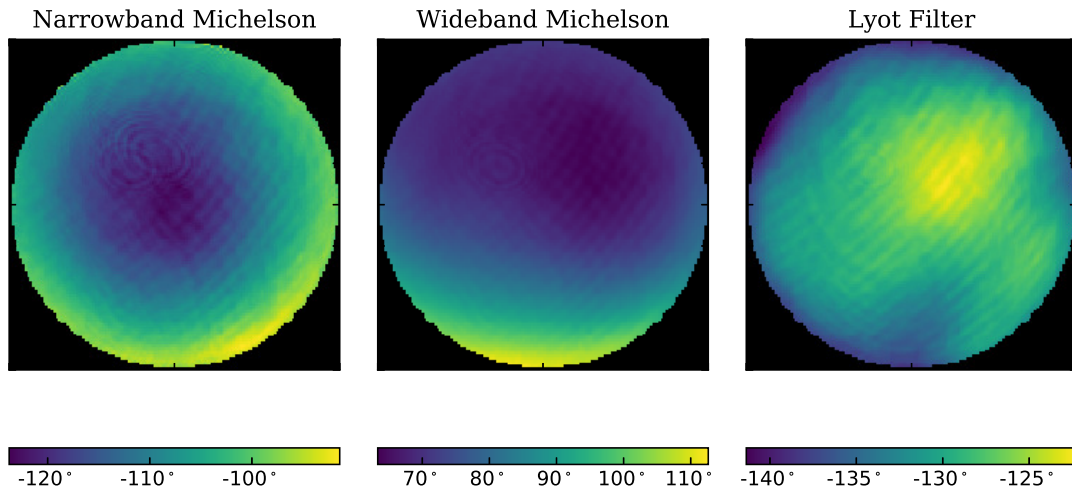
Figure 12: Example phasemaps for the three tunable elements in the HMI filter section. The phasemaps shown are for camera 2, taken on 2021 July 9. These phasemaps were used to compute the look-up tables shown in Figure 17. The phasemaps shown here have been corrected for the front window fringes.

determined every two weeks on orbit. Monitoring changes in these maps are used to determine when to change the instrument tuning, as well as calculate the look-up tables used to generate science data products (see section 5.3).

The observing sequence used is referred to as a detune sequence, and is generally done in CALMODE, with the instrument imaging the entrance pupil rather than the Sun. This minimizes the effects of variation in the solar line over the field, but involves a different optical path through the instrument. The phases determined in CALMODE need to have corrections applied before being used to calibrate OBSMODE observations. The detune sequence consists of a series of observations with each wavelength selector rotated to one of three positions, 120° apart. There are thus 27 total detune positions, and they are taken with both cameras. The phasemaps are determined separately for each camera, and show some differences, possibly due to the beamsplitter immediately before the cameras in the optical path. Because the phases vary slowly over the field, the data are binned down to a smaller grid size to improve signal to noise and computation time. The standard processing computes the phases and line parameters on a 128×128 grid.

One particular problem that is introduced by using CALMODE rather than OBSMODE is that the front window and blocking filter have interference fringes caused by their contruction from layers of materials with differing optical properties. In OBSMODE, these fringes are averaged across the entire field but in CALMODE, where they are imaged at the CCDs, these fringes are picked up clearly. A more complete description

of these fringes can be found in S. Couvidat et al. (2016); in this section we discuss how they are corrected in the phasemaps.

The fringes $\mathcal{A}(\mathbf{x}, t)$ are modeled as

$$\mathcal{A}(\mathbf{x}, t) = \mathcal{A}_{\mathrm{C}}(\mathbf{x}) \cos\left(\phi(t)\right) + \mathcal{A}_{\mathrm{S}}(\mathbf{x}) \sin\left(\phi(t)\right) \tag{21}$$

where $\mathcal{A}_{\mathrm{C}}$ and $\mathcal{A}_{\mathrm{S}}$ are the amplitudes of the fringes which are arbitrary functions of field position, and $\phi(t)$ describes the phase of the fringes which varies with time. The fringe correction 21 is determined by assuming that each phasemap $\Phi_i(\mathbf{x})$ is a mean and linearly varying function of time plus the fringes $\mathcal{A}(\mathbf{x}, t)$. An initial guess is made from the line width fits, then the solution is iteratively improved, and finally subtracted from the phasemaps.

4.9   Polarization

Accurately characterizing the polarization performance of the HMI instrument is critical for generating all of HMI's science data products. The design, theoretical performance, and calibration of HMI is described in detail in J. Schou, Borrero, et al. (2012) and on-orbit experience is further discussed in S. Couvidat et al. (2016). The solar light that reaches the HMI instrument can be represented by the Stokes vector $\mathrm{I}_{\mathrm{sun}} = [I, Q, U, V]$ which completely describes the polarization of the beam that enters the instrument. Neglecting losses due to transmission less than unity, the light $\mathrm{I}_{\mathrm{HMI}}$ that reaches the camera detectors at the far end of the optical path is modified by the effects of the various optical elements of the instrument. The total effect can be described in a 4×4 modulation matrix $\mathcal{O}$:

$$\mathrm{I}_{\mathrm{HMI}} = \mathcal{O}\mathrm{I}_{\mathrm{sun}}. \tag{22}$$

Recovering the true Stokes vector requires applying the demodulation matrix $\mathcal{D} = \mathcal{O}^{-1}$ to the data:

$$\mathrm{I}_{\mathrm{cor}} = \mathcal{D}\mathrm{I}_{\mathrm{HMI}} = \mathcal{D}\mathcal{O}\mathrm{I}_{\mathrm{sun}}. \tag{23}$$

The modulation matrix must be determined with significant accuracy to achieve HMI's science requirements. If we define the error matrix $\mathcal{E} = \mathcal{D}\mathcal{O}_{\mathrm{true}} - \mathcal{I}$, where $\mathcal{O}_{\mathrm{true}}$ is the true modulation matrix and $\mathcal{I}$ is the identity matrix, then we require the absolute values of $\mathcal{E}$ to be less than

$$\mathcal{E}_{\mathrm{max}} = \begin{pmatrix} 0.01 & 0.1 & 0.1 & 0.1 \\ 0.001 & 0.01 & 0.01 & 0.01 \\ 0.001 & 0.01 & 0.01 & 0.01 \\ 0.001 & 0.01 & 0.01 & 0.01 \end{pmatrix} \tag{24}$$

The adequacy of these upper bounds is discussed in J. Schou, Borrero, et al. (2012). In this section we discuss the determination of the modulation matrix, and further corrections that are applied to the data.

The modulation matrix determined for the HMI instrument is modelled as the combined effects of the telescope, the polarization selectors, and the polarizing beamsplitter. Other sources of polarization demodulation or cross-talk, such as the focus blocks or ISS mirror, have been determined to have negligible impact and so are not included in the modulation matrix. The modulation matrix, therefore, is given by

$$\mathcal{O} = \mathcal{M}_{\mathrm{tel}} \times \mathcal{M}_{\mathrm{sel}} \times \mathcal{M}_{\mathrm{bs}}, \tag{25}$$

where $\mathcal{M}_{\mathrm{tel}}$ is the Mueller matrix for the telescope optical element, $\mathcal{M}_{\mathrm{sel}}$ is the Mueller matrix for the polarization selectors, and $\mathcal{M}_{\mathrm{bs}}$ is the Mueller matrix for the polarizing beamsplitter.

The telescope consists of the front window, a primary lens, and a secondary lens. The front window and primary lens are close enough together as to be indistinguishable in this model. The secondary lens is somewhat separated in the optical path; nevertheless we consider all three as a single optical element. The telescope acts as a depolarizer and the

front window is somewhat birefringent. The front window and primary lens are mounted
to the telescope tube in a mounting ring that is thermally controlled, with heaters on the
top and bottom. The temperature of the mounting ring (and therefore of the window
and primary lens) varies with time, and this affects the birefringence. The telescope
is modeled as a six-element Mueller matrix which accounts for both depolarization and
retardance:

$$
\mathcal{M}_{\text{tel}} = \begin{pmatrix}
1 & 0 & 0 & 0 \\
0 & M_{QQ} & M_{QU} & M_{QV} \\
0 & M_{QU} & M_{UU} & M_{UV} \\
0 & -M_{QV} & -M_{UV} & M_{VV}
\end{pmatrix}.
\tag{26}
$$

The diagonal terms have been found to be temperature dependent. The closest avail-
able measurable T_{front} being the temperature measured at the telescope front window
mounting ring. The temperature dependent terms are reasonably well-described by a
quadratic in $T = T_{\text{front}} - 24°\text{C}$. The matrix $\mathcal{M}_{\text{tel}}$ therefore has twelve parameters, which
are determined on a 32×32 grid.

The polarization selectors are three rotating elements with nominal retardances of
10.50, 10.25, and 10.50 wavelengths, in the order encountered in the optical path. These
are referred to as PS1, PS2, and PS3, respectively. They are each modelled as perfect
retarders with fast axis angle ϕ and retardance r:

$$
W(\phi, r) = \begin{pmatrix}
1 & 0 & 0 & 0 \\
0 & c^2 + s^2 \cos\delta & cs(1 - \cos\delta) & -s \sin\delta \\
0 & cs(1 - \cos\delta) & s^2 + c^2 \cos\delta & c \sin\delta \\
0 & s \sin\delta & -c \sin\delta & \cos\delta
\end{pmatrix},
\tag{27}
$$

where $c = \cos 2\phi$, $s = \sin 2\phi$, and $\delta = 2\pi r$. This model is valid only for normal incidence:
for non-zero incidence, the retardance can be modified as

$$
r' = r \left(1 + \alpha^2 \cos\left(2(\beta - \phi)\right)/2 \right),
\tag{28}
$$

where α is the incidence angle and $\beta - \phi$ is angle between the fast axis of the element and
the direction to the center of the field. As with the telescope polarization performance,
the polarization selector performance has been found to be temperature-dependent. A
linear dependence on the temperature measured at the polarization selectors is used for
the retardances, and so the retardance used for each selector is $r_i = r(T_{\text{sel}}, \alpha, \beta)$. The
polarization selector Mueller matrix is therefore

$$
\mathcal{M}_{\text{sel}} = W_{\text{PS1}}(\phi_1, r_1) \times W_{\text{PS2}}(\phi_2, r_2) \times W_{\text{PS3}}(\phi_3, r_3).
\tag{29}
$$

As with the telescope matrix, the parameters for this matrix have been determined on a
32×32 grid.

The polarizing beamsplitter selects vertically polarized light to be sent to the filter
section of the instrument and to the cameras. The other beam is sent to the ISS sensors.

	mean	T	T^2
M_{QQ}	1.001805	6.1596×10^{-4}	-4.4283×10^{-4}
M_{UU}	0.997478	1.4866×10^{-4}	-4.2629×10^{-4}
M_{VV}	1.000953	4.9386×10^{-4}	-8.5552×10^{-4}
M_{QU}	-0.003701		
M_{QV}	-0.001460		
M_{UV}	-0.004462		

Table 5: Mean values for the elements of the telescope Mueller matrix $\mathcal{M}_{\text{tel}}$. Linear and quadratic corrections for front window temperature are shown for the diagonal elements.

	$I \to Q$	$I \to U$	$I \to V$
r^0	2.0411683e-06	-0.00011803840	4.2255156e-06
r^1	0.00012040193	0.00011883301	1.7374540e-05
r^2	0.00026537064	0.00023335908	1.3426406e-05
r^3	-0.00059574417	-0.0011413839	0.00012586214
r^4	-0.0026085394	-0.0034897879	0.00045829690

Table 6: Coefficients for leakage of I into Q, U, V, as a function of distance r from the center of the field.

The beamsplitter is modelled as a pure linear polarizer with angle θ and transmission t:

$$P(\theta, t) = \frac{t}{2} \begin{pmatrix} 1 & \cos 2\theta & \sin 2\theta & 0 \\ \cos 2\theta & \cos^2 2\theta & \cos 2\theta \sin 2\theta & 0 \\ \sin 2\theta & \cos 2\theta \sin 2\theta & \sin^2 2\theta & 0 \\ 0 & 0 & 0 & 0 \end{pmatrix}. \tag{30}$$

The beamsplitter is assumed to be perfect. Because the beam is not telecentric, a slight dependence on field position in the polarization direction exists. This is treated as a slight variation in θ with vertical position, varying from approximately $-1°$ to $1°$.

The above-described modulation matrix does not account for leakage from I into Q, U, and V, and so this leakage is determined separately. The leakage is a function of distance from field center, and is approximated with a forth-order polynomial.

4.9.1   Ground Calibration

Determination of the modulation matrix $\mathcal{O}$ was done during pre-launch calibration operations, using the stimulus telescope and the Polarization Calibration Unit (PCU). A full description of the setup and calibration of the test apparatus can be found in J. Schou, Borrero, et al. (2012). In brief, the PCU calibration setup allows light of a known polarization state to be passed through the HMI instrument in various configurations. By taking sequences of varying polarization states, and changing the instrument configuration, the various unknown quantities can be fit for.
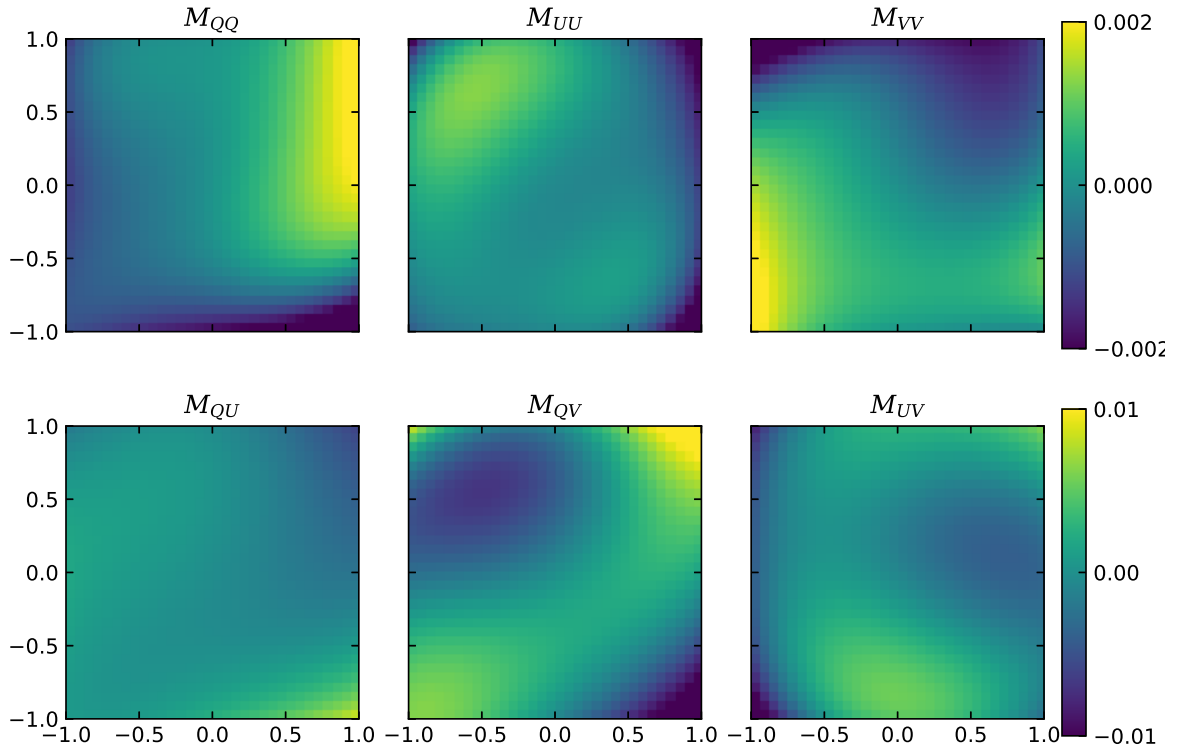
Figure 13: Variation of the six elements of $\mathcal{M}_{\text{tel}}$ across the field. The mean values are given in Table 5.

The components of the matrix 26 were fit at each pixel and then averaged over a 32×32 grid. The mean values of each parameter are given in Table 5, and the variations from the mean over the field are shown in Figure 13. The calibration sequences were taken over a variety of front window and ambient temperatures, allowing for the temperature dependence of the elements of matrix 26 to be determined. It was found that the only the diagonal elements (the depolarization terms) had any significant temperature sensitivity, and this could be well approximated with a quadratic correction. The coefficients were determined over the same 32×32 grid, and the mean values are shown in Table 5. The thermal coupling of the front window and primary lens in air is different from the thermal coupling in a vacuum (ground calibration tests for polarization were not done in a vacuum due to the added optical effects of the vacuum chamber window) and this introduces some uncertainty into the polarization calibration.

For each polarization selector, two parameters must be determined: the orientation ϕ_i of the fast axis, and the true retardance r_i. As with the telescope parameters, these parameters were determined over a 32×32 grid. These angles are the orientations of the fast axes when the motors that rotate the polarization selectors are moved to their zero
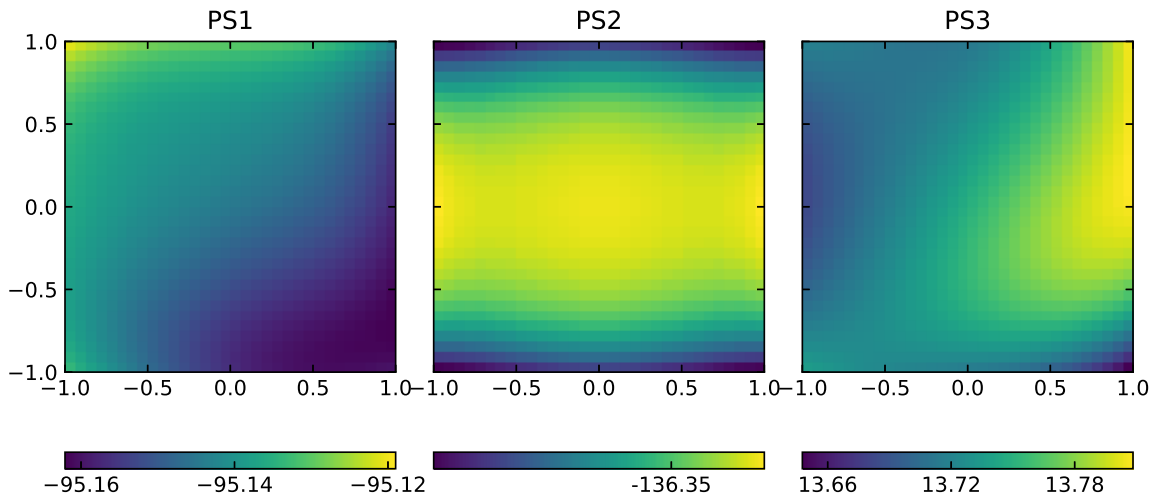
Figure 14: Angles Φ_i of the fast axis determined for each polarization selector, in degrees. The variation across the field for PS2 is essentially zero.

position. Each motor can rotate to 240 discrete stopping points with the actual position telemetered back as an integer PS$i \in [0, 239]$. The angle ϕ_i in the matrix 27 is given by

$$\phi_i = \Phi_i + \text{PS}i \times \text{step}_i, \tag{31}$$

where $\text{step}_i = -1.5°$ for PS1 and PS2 and $\text{step}_3 = 1.5°$ for PS3. The angles Φ_i determined during pre-launch calibrations are shown in Figure 14.

The mean retardances were found to be 10.496, 10.248, and 10.494 for PS1, PS2, and PS3, respectively. The variations across the field from these means are shown in Figure 15. In addition, it was found that these retardances are sensitive to temperature, and so a linear correction as a function of $T = T_{\text{sel}} - 22°C$ was determined. These coefficients are also shown in Figure 15.

4.9.2 On-Orbit Calibration

The leakage from I into Q, U, and V, or the telescope polarization, was determined from on-orbit observations. It was found that the leakage of I into the linear polarization states was well-described by a quadratic function of distance from field center. The coefficients of the functions fit for leakage into Q, U, and V are shown in Table 6. After the correction of this leakage, a further systematic was discovered — a granulation-like pattern in Q and U. While the origin of this systematic is not well understood, it may be due to slightly different PSFs in different observing configurations. From on-orbit observations, a 5×5 kernel was determined that, when convolved with I, best reproduces the observed Q and U. These kernels are shown in figure 16.
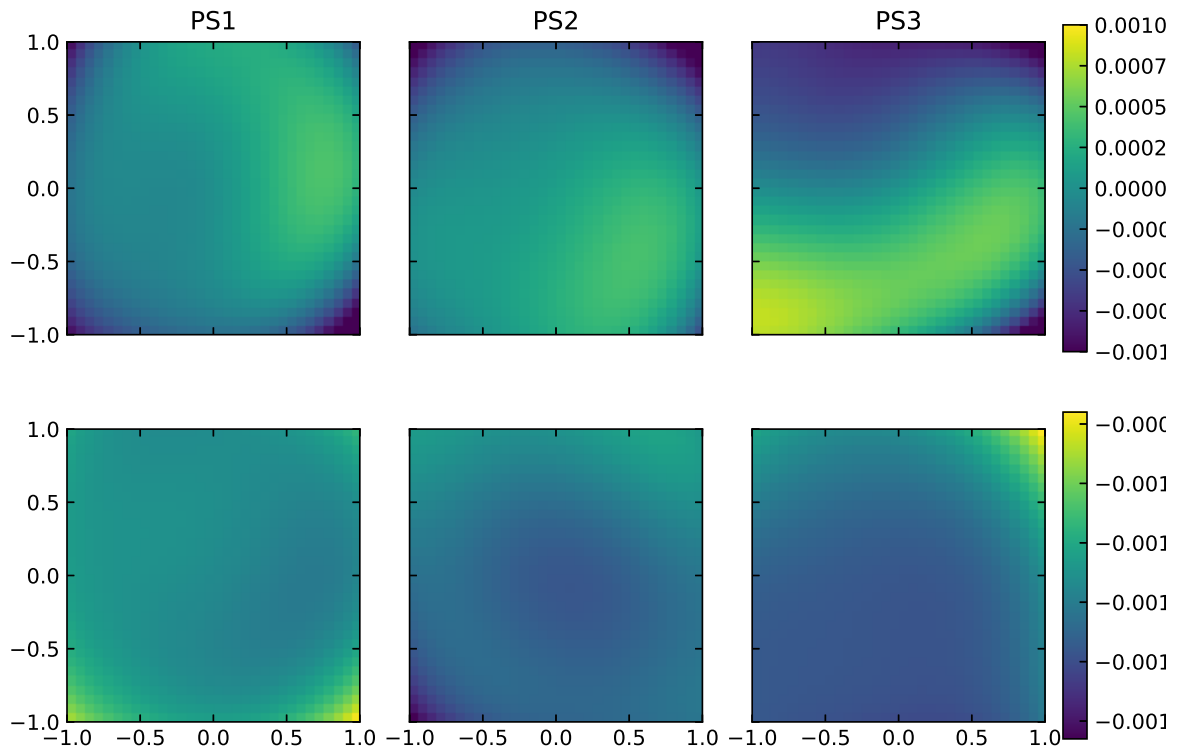
Figure 15: Retardances for the polarization selectors. The top row shows the variation relative to the mean for each of the polarization selectors. The bottom row shows the linear correction for temperature determined during the ground calibration phase.
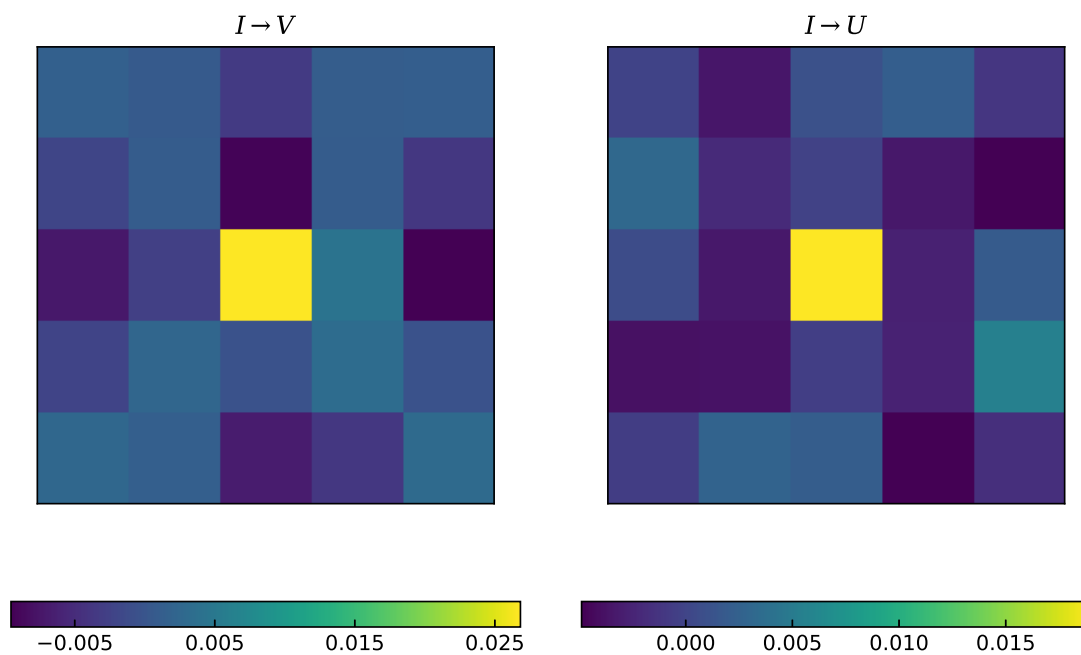
Figure 16: Kernels used to correct for polarization-dependent PSF.

5 HMI Measurement Algorithms — Calibrated Filtergrams to Observable Quantities

The calibrated filtergrams are used to compute more useful physical quantities called *observables*. There are two sets of basic observables - the Stokes parameters (I Q U V) that are inverted to determine the vector magnetic field and other thermodynamic quantities and the more straightforward line-of-sight observables: velocity, magnetic field, continuum intensity, line depth, and line width.

5.1 Algorithm Theoretical Basis

The primary level 1 HMI measurement is high-resolution, extremely narrow band-pass images, in all four Stokes parameters. The image is focused on the detectors by a series of lenses, planar optical elements, and mirrors. Wavelength selection is accomplished by passing the light through a set of fixed and tunable filters. Polarization selection is accomplished by fixed and rotating polarizing elements. The solar photons that traverse the optical system are converted in to electrical signals by the two CCD cameras, which are read out, assembled into telemetry packets and sent to the ground for reconstruction and calibration. The absolute photon counts, or irradiances, received at the detectors is not required, so the final measurements are given in signal units (DN).

The measurement algorithms thus consist of corrections to the raw signal counts for detector bias, linearity, and pixel-to-pixel variations, removal of artifacts, corrections for errors in the polarization selection, and determination of quantities necessary for further analysis, in particular the transmission as a function of wavelength at each position in the image, and the image coordinates and scale. Almost all of these steps require quantities derived from the calibrations described in section 4.

5.2 Conversion of Instrument Signals to Stokes I,Q,U,V

The generation of calibrated filtergrams begins with raw level-0 filtergrams and a set of calibration data sets, and ends with either LCP/RCP intensity measurements or with Stokes I, Q, U, V vectors. The level 1.5 science data products that HMI produces are either at 45 second cadence (which employ the LCP/RCP filtergrams) or at 12 minute cadence (which use the Stokes vectors). The former data products include the line-of-sight magnetograms and Dopplergrams, while the latter data products include the vector magnetic field products. The calibrations used are derived in the same ways in either case, but there are some differences in which corrections are applied. The LCP/RCP filtergrams are not usually archived after the level 1.5 data products are computed; the I, Q, U, V filtergrams are also level 1.5 data products and are saved. In addition, near-real-time (NRT) data products are produced as quickly as possible and made available for users that require current data. Level 1 data are generally available within 5 minutes of the observations being taken on the spacecraft, while level 1.5 data generally lag by

about 20 minutes (for 45s cadence products) or 50 minutes (for 720s cadence products). In general, the NRT data products are produced using the same algorithms as the definitive data, but some corrections are skipped or applied with less precision. Level 1.5 data definitive data products also employ some corrections computed from the NRT data sets. NRT products are also sometimes subject to missing data that are back-filled before the definitive data products are computed.

5.2.1   Image Corrections

Image corrections are applied to HMI filtergrams at various points throughout the science data processing pipeline. The order in which they are applied is interspersed with other corrections and calibrations, and that order is made explicit in Appendix F, but they are discussed together in this section.

The first steps in image correction are to remove the overscan rows from the level 0 filtergrams and to apply corrections for image corruption, if needed an possible. Image corruption occurs due to errors in the camera electronics that occur occasionally, and in some cases can be reversed. Where these errors occur and correction is not possible, a quality bit is set in the metadata. Once this is done, the following corrections are applied

5.2.1.1   CCD Corrections   Each filtergram needs to be corrected for bias and gain variations across the field, and is normalized for exposure time. The bias correction, or dark current, is monitored every day but is not seen to vary (see section 4.6.2). The gain correction is contained the flat field, which is updated every week. The image pixels $I_1(\mathbf{x})$ in a level 1 filtergram are computed from the level 0 filtergram pixels $I_0(\mathbf{x})$ by:

$$I_1(\mathbf{x}) = (I_0(\mathbf{x}) - I_D(\mathbf{x}))/(F(\mathbf{x}) \cdot \tau_{\mathrm{exp}}) \tag{32}$$

where $I_D(\mathbf{x})$ is the dark frame, $F(\mathbf{x})$ is the flatfield, and τ_{exp} is the exposure time.

5.2.1.2   Cosmic Ray and Bad Pixel Removal   Permanent bad pixels and ephemeral spikes, generally caused by high energy particle hits to the detectors, are detected and removed. Permanent bad pixels are known before the filtergram is analyzed (see section 4.6.1), while cosmic ray hits are detected during science data processing in two passes. The first is done by analyzing individual filtergrams and looking for large excursions relative to neighboring pixels, the second is done by looking at sequences of filtergrams and finding temporal excursions. The latter detection is not done on NRT records.

Cosmic ray hits to pixels within image $I(\mathbf{x})$ are inferred by comparing a temporary high-pass version $I_{\mathrm{H}}(\mathbf{x})$ to an empirical threshold computed from the $I_{\mathrm{H}}(\mathbf{x})$ centroid. The high-pass is created by first constructing a low-pass version $I_{\mathrm{L}}(\mathbf{x})$ via convolution of the incoming $I(\mathbf{x})$ with a gaussian kernel $f(d)$ defined as,

$$f(d) = A \exp^{-(d/\sigma_{\mathrm{L}})^2/2} \tag{33}$$

where d is (integer) pixel index, σ_{L} is low-pass kernel width,

$$\sigma_{\mathrm{L}} = \frac{1}{2\sqrt{2\log(2)}} = 0.4247 \tag{34}$$

and A is determine such that $\sum f(d) = 1$ over support range $-n \leq d \leq +n$, with $n = 4$. Sequential 1d convolutions are performed first in x and then y to create low-pass $I_{\mathrm{L}}(\mathbf{x})$, whereafter $I_{\mathrm{H}}(\mathbf{x})$ is formed by simple subtraction, $I_{\mathrm{H}}(\mathbf{x}) = I(\mathbf{x}) - I_{\mathrm{L}}(\mathbf{x})$.

With original image $I(\mathbf{x})$ in hand and high-pass version $I_{\mathrm{H}}(\mathbf{x})$ so obtained, a limited central region Ω is then defined as fixed fraction of total image size within which the average intensity of $I(\mathbf{x})$ and standard deviation of $I_{\mathrm{H}}(\mathbf{x})$ are computed as,

$$I_{\mathrm{avg}} = \frac{1}{N} \sum_{\Omega} I(\mathbf{x}) \tag{35}$$

and,

$$\sigma_{\mathrm{H}} = \left[\frac{1}{N} \sum_{\Omega} I_{\mathrm{H}}(\mathbf{x})^2 \right]^{\frac{1}{2}} \tag{36}$$

where N is count of points in Ω. Then provided I_{avg} and σ_{H} fall within reasonable limits, a cosmic hit is declared for any pixel for which,

$$I(\mathbf{x}) > 10.5 \cdot \sigma_{\mathrm{H}} \quad \text{or} \quad I(\mathbf{x}) > 90\% \text{ max value} \tag{37}$$

The resulting cosmic hit list is then merged with the permanent bad pixel list (see section 4.6.1) and the complete list of bad pixels are passed to the gap-filling routine to be fixed.

Both permanently bad pixels and transient spikes are treated in the same way. The gap-filling algorithm replaces bad pixels with values obtained by least-squares fit to neighboring good pixels weighted by the instrument spatial autocorrelation function. Each pixel neighborhood has fixed size 80×80 centered on the bad pixel to be fixed. Ideally, each bad pixel is the only one within its neighborhood, but to deal with the case where additional pixels may be missing within the vicinity of the pixel being filled, the autocorrelation matrix is first modified by deleting the row and column of other missing pixels prior to calculating the filled pixel value. In all cases, the filled pixel value makes best use of available data while avoiding skew introduced by any nearby missing pixels.

5.2.2 Combining Filtergrams

Most HMI science data products involve information from more than one observed filtergram. Combining multiple observations into a single measurement requires spatially and temporally co-registering two or more filtergrams, taking in to account differences in pointing and plate scale, distortion, and observing time. Account must also be taken of fact that the Sun has a different apparent radius depending on the wavelength observed, and that the Sun rotates between observations.

The choices of target times and image coordinates varies with the output data product, as does the choice of input. The standard HMI data products are output on either a 45 second or 720 second cadence, and are done either as a quick look, or NRT, data product, or as definitive data.

5.2.2.1 Image Coordinate Determination   The image coordinates are determined by finding the center of the solar disk and fitting the solar limb. The plate scale in

arcseconds per pixel is then computed using the known distance of the Sun from the spacecraft. For computational efficiency the input filtergram is binned down by a factor of 4 to a 1024×1024 image. A high-pass filter is applied to an annulus with an inner radius of 85% of the image radius and out radius equal to the image radius:

$$
I_{\mathrm{H}}(\mathbf{x}_i) = \begin{cases} \sqrt{(I(x_{i-1}, y) - I(x_{i+1}, y))^2 + (I(x, y_{i-1}) - I(x, y_{i+1}))^2} & \text{if } 0.85\frac{n_x}{2} < r < \frac{n_x}{2} \\ 0 & \text{otherwise} \end{cases}
\tag{38}
$$

where $r = |\mathbf{x} - \mathbf{x}_{\mathrm{cen}}|$ and n_x is the number of pixels in the horizontal direction. The center position of the solar disk is determined by cross-correlating I_{H} with itself mirrored in x and y. The maximum of the cross-correlation is estimated by quadratic interpolation, and this is used to compute the disk center in image coordinates. The filter image $I_{\mathrm{H}}(\mathbf{x})$ can be remapped to $I_{\mathrm{H}}(r, \theta)$, where r is the distance from disk center in pixels and θ is the polar angle. The number of points in θ is chosen to be one fourth of the approximate number of pixels around the solar limb, which amounts to approximately 3000 radial slices, each of which is fit independently. For each θ_i, the maximum pixel value $I_{\mathrm{H}}(r_{\max}, \theta_i)$ is found. A quadratic function is fit over a small window $r = [r_{\min}, r_{\max}]$:

$$
\left(1 - \cos\left(\frac{r - r_{\max}}{2\pi(r_{\max} - r_{\min})}\right)^4\right) \sum_{k=0}^{2} a_k r^k.
\tag{39}
$$

The estimate of the maximum can then be refined as $r_{\max} = -a_2/2a_1$. The window used is 8 pixels on either side of the maximum. All valid fits are averaged to get a single value for the disk radius, and if more than 75% of the attempted fits were successful the limb fit value is used. If this criterion is not met, the limb fit function fails and the filtergram is not used in subsequent data processing.

The apparent radius of the Sun changes by a few hundred kilometers depending on which part of the solar FeI line is observed (Fleck, S. Couvidat, and Straus, 2011; Emilio et al., 2015). This causes an apparent but spurious change in the image plate scale. To correct this problem, a correction to the radius returned by the limb finder is applied:

$$
\Delta R = A \exp\left(-(wl_{\mathrm{X}} - wl_0)^2/wl_{\mathrm{W}}\right),
\tag{40}
$$

where $A = 0.445$, $wl_0 = 0.25$, and $wl_{\mathrm{W}} = 7.1$. The value of $wl_{\mathrm{X}} = wl - v_{\mathrm{obs}}/dvdw$, where $dvdw = \delta\lambda/\lambda \times c$, v_{obs} is the velocity of the spacecraft along the line of sight, and wl is an index that for the normal observing sequence is $wl \in [-5, -3, -1, 1, 3, 5]$. A correction is made to the image center $\mathbf{x}_{\mathrm{cen}} = (x_{\mathrm{cen}}, y_{\mathrm{cen}})$:

$$
\Delta x_{\mathrm{cen}} = -\frac{d\Delta R}{dwl_{\mathrm{X}}} \cos(180° - \theta)
$$
$$
\Delta y_{\mathrm{cen}} = -\frac{d\Delta R}{dwl_{\mathrm{X}}} \sin(180° - \theta),
\tag{41}
$$

where $wl_0 = 0.35$, $wl_{\mathrm{W}} = 6.15$, and θ is the image rotation angle.

mean	2.7139
$\sin^2 \mathrm{lat}$	-0.405
$\sin^4 \mathrm{lat}$	-0.422

Table 7: Coefficients for differential rotation correction. Units are microradians / second.

5.2.2.2 Spatial Interpolation: Distortion Correction, Co-Registration, and De-Rotation

Each filtergram in a set is interpolated to a common plate scale and image center, with the known distortion removed, and optionally with the solar differential rotation removed as well. This is done in a single pass, with the corrected filtergram $I_{\mathrm{cor}}(\mathbf{x})$ interpolated from the original filtergram $I(\mathbf{x}')$, and the pixels shifts $\mathbf{x}'$ the sum of the distortion, image shift, and rotation correction:

$$\mathbf{x}' = \mathbf{x} + \mathbf{a}_{\mathrm{dist}} + \mathbf{a}_{\mathrm{shift}} + \mathbf{a}_{\mathrm{rot}}. \tag{42}$$

The distortion correction $\mathbf{a}_{\mathrm{dist}}$ is described in section 4.5.1, and is different for each camera. The target coordinates for the shift are chosen as the median of the image centers and image scale, with images whose center differ from the target center by more than 5 pixels, or whose apparent solar radius differs by more than 9.1 pixels, are rejected.

De-rotation is applied to the filtergrams as well if any of the following conditions are met: if the P-angle (orientation of solar north in each image) varies by more than $0.0028°$ across all the input images, if the B-angle (solar inclination varies by more than $0.05°$ across all images, if the image centers in x or y vary by more than 1 pixel, or if the apparent solar radius varies by more than 0.1 pixel. If the derotation correction is applied, the coordinates $\mathbf{x}$ for every input image are deprojected, a differential rotation profile that is forth order in $\sin \mathrm{lat}$ is applied, and then the coordinates projected to a common B- and P- angle $\mathbf{a}_{\mathrm{rot}}$. The coefficients used in the differential rotation profile are given in table 7. In practice, this correction is applied to all filtergrams used in level 1.5 data products.

5.2.2.3 Temporal Interpolation

Temporal interpolation is done after the spatial interpolations have been done on all the filtergrams in a set. The target time is set by the cadence of the output data set, which is either 45 seconds or 720 seconds for normal HMI data products. For the LOS observables on a 45 second cadence, the target time is chosen computed for a distance of precisely 1AU, so the actual observed time interpolated to is the target time plus a correction that equals $(1 - d_{\mathrm{sun}}) * d_{\mathrm{AU}}/c$, where d_{sun} is the distance between the spacecraft and the Sun in AU, d_{AU} is 1AU, and c is the speed of light. This ensures that the temporal cadence is uniform for long time series analysis. The target time for 720s products is the time at the spacecraft's position. For 45s filtergrams, 6 images are used for the temporal interpolation which corresponds to 4.5 minutes of data (only 2 are used for NRT filtergrams), whereas for 720s filtergrams, 10 or 14 images are used for mod C and mod L observations, respectively (22.5 or 21 minutes of data).

5.2.3 Polarization Corrections

The input HMI observations are sets of filtergrams taken with different instrument polarization settings $I_{\mathrm{obs}} = [I_0, \ldots, I_{N_{\mathrm{pl}}-1}]$, where N_{pl} is the number of different polarization observations. From these we obtain images corrected for the instrument polarization characteristics; either stokes vectors $\mathrm{I}_{\mathrm{cor}} = [I, Q, U, V]$ or pairs of circularly polarized filtergrams $I_{\mathrm{cor}} = [I_{\mathrm{LCP}}, I_{\mathrm{RCP}}]$. These are obtained by applying the demodulation matrix $\mathcal{D}$:

$$\mathrm{I}_{\mathrm{cor}} = \mathcal{D}\mathrm{I}_{\mathrm{obs}}, \tag{43}$$

which is determined with knowledge of the instrument modulation matrix $\mathcal{O}$ discussed in section 4.9. For the line-of-sight observables, only circularly polarized input filtergrams are used, so the rows and columns with the linear polarization states are deleted from the matrices, the modulation and demodulation matrices become 2×2 matrices, and the leakage from Q and U is not accounted for. The polarization correction is done in four steps: first the modulation matrix $\mathcal{O}$ is determined and inverted to obtain the demodulation matrix $\mathcal{D}$. Then the demodulation matrix is interpolated to the pixel grid of the desired output images and applied to the input data. A correction for the telescope polarization is then applied, and finally a correction for the polarization-dependent PSF.

The various parameters that are needed to compute the modulation matrix have been determined on a 32×32 grid, and so the modulation and demodulation matrices are determined at each of those 1024 points, and then interpolated to needed pixel location. The elements of the telescope Mueller matrix $\mathcal{M}_{\mathrm{tel}}$ (26) are read in first. The linear and quadratic terms in front telescope temperature are set to zero, so no temperature-dependent correction is made. Then, for each of the j input filtergrams (either two or four), a separate modulation matrix is computed as

$$\mathcal{O}_j = \mathcal{M}_{\mathrm{tel}} \times W_{\mathrm{PS1}}(\theta_1, r_1') \times W_{\mathrm{PS2}}(\theta_2, r_2') \times W_{\mathrm{PS3}}(\theta_3, r_3') \times P(90° + y1.0525°, 1), \quad (44)$$

with the retarder matrices defined in equation 27 and the modified retardances from equation 28. The vertical position in the field y runs from -1 to 1. For NRT data, the temperature $T_{\mathrm{sel}} = 20°\mathrm{C}$. For definitive data the temperature used is the five minute average of the thermistor closest to the polarization selectors (the ID for this thermistor is TS08). The corrections are shown in Figure 15.

Equation 22 uses the modulation matrix to convert from the stokes vector $\mathrm{I}_{\mathrm{sun}}$ to the stokes vector at the dector $\mathrm{I}_{\mathrm{HMI}}$, but the actual measurements are the observed filtergrams $\mathrm{I}_{\mathrm{obs}}$ which are the stokes I for each instrument polarization setting. The modulation matrix $\mathcal{O}_{\mathrm{obs}}$ is required such that

$$\mathrm{I}_{\mathrm{obs}} = \mathcal{O}_{\mathrm{obs}}\mathrm{I}_{\mathrm{sun}}. \tag{45}$$

The jth row of the matrix $\mathcal{O}_{\mathrm{obs}}$ is the top row of the modulation matrix $\mathcal{O}_j$ for the polarization settings for the jth filtergram in $\mathrm{I}_{\mathrm{obs}}$. This matrix is inverted using Cholesky facotrization to obtain $\mathcal{D}$.

Now the output filtergrams I_{cor} can be computed. At each pixel location $\mathbf{x}$, the demodulation matrix $\mathcal{D}(\mathbf{x})$ is determined by bilinear interpolation. Then the output filtergrams $I_i \in I_{cor}$ are computed by

$$I_i(\mathbf{x}) = 0.5 \sum_{j=0}^{N_{pl}-1} I_j \mathcal{D}_{ij}(\mathbf{x}), \tag{46}$$

where the leading factor of 0.5 scales the output intensity to be equal to the input. Next the effect of telescope polarization is accounted for. The correction is forth order in distance from field center $r = |\mathbf{x}|$ where the image radius is normalized to 1. The coefficients are given in Table 6. The leakage is calculated at each pixel for Q and U and subtracted from the filtergrams. The leakage into Stokes V and I_{LCP}, I_{RCP} are not corrected as the telescope introduces very little circular polarization into the beam. Finally, the polarization-dependant PSF is corrected for in Q and U. The kernels shown in Figure 16 are convolved with the intensity filtergram I and then subtracted from the Q and U filtergrams.

5.3 HMI Line-Of-Sight Observables

The primary line-of-sight (LOS) science data generated by the HMI project is a set of scalar parameters computed over the entire solar disk: continuum intensity, LOS velocity (Dopplergrams), LOS magnetic field (flux density), computed intensity at the core of the FeI line, and the width of the same line. These data are generated at the full HMI resolution, stored as 4096×4096 pixel images, and computed at two standard cadences: 45 seconds and 12 minutes. These data are referred to as LOS 'observables' and are the lowest level data product that most end users of HMI data ever see. The inputs to the 45 second and 12 minute data products differ in some respects, but the algorithm to compute these five observable quantities is the same in either case, and is described in this section. The algorithm is developed from the one used on the MDI instrument, and is therefore commonly referred to as the 'MDI-like' algorithm.

5.3.1 Algorithm description

The MDI-like algorithm begins with computing the first and second Fourier coefficients a_n and b_n of the FeI line profile $I(\lambda)$:

$$a_1 = \frac{2}{\tau} \int_{-\frac{\tau}{2}}^{\frac{\tau}{2}} I(\lambda) \cos 2\pi \frac{\lambda}{\tau} d\lambda; \qquad b_1 = \frac{2}{\tau} \int_{-\frac{\tau}{2}}^{\frac{\tau}{2}} I(\lambda) \sin 2\frac{\lambda}{\tau} d\lambda \tag{47}$$

$$a_2 = \frac{2}{\tau} \int_{-\frac{\tau}{2}}^{\frac{\tau}{2}} I(\lambda) \cos 4\pi \frac{\lambda}{\tau} d\lambda; \qquad b_2 = \frac{2}{\tau} \int_{-\frac{\tau}{2}}^{\frac{\tau}{2}} I(\lambda) \sin 4\frac{\lambda}{\tau} d\lambda, \tag{48}$$

where τ is the period of the observation span. In the standard observing sequence with 6 wavelength positions with nominal separations of 68.8mÅ, $\tau = 412.8$mÅ. Under the assumption that the true solar FeI line is a Gaussian with continuum intensity I_c, line depth I_d, a full-width half-max given by $\text{FWHM} = 2\sqrt{\log(2)}\sigma$, and a Doppler shift λ_0:

$$I(\lambda) = I_c - I_d \exp\left(-\frac{(\lambda - \lambda_0)^2}{\sigma^2}\right). \tag{49}$$

The Doppler velocity v is given by the phase of the Fourier coefficients, scaled to obtain the correct physical units:

$$v = \frac{dv}{d\lambda} \frac{\tau}{2\pi} \arctan\left(\frac{b_1}{a_1}\right), \tag{50}$$

where $dv/d\lambda = 48562.4\text{ms}^{-1}\text{Å}^{-1}$. The line width σ can be computed by

$$\sigma = \frac{\tau}{\pi\sqrt{6}} \sqrt{\log\left(\frac{a_1^2 + b_1^2}{a_2^2 + b_2^2}\right)}, \tag{51}$$

and the line depth I_d is given by

$$I_d = \frac{\tau}{2\sigma\sqrt{\pi}} \sqrt{a_1^2 + b_1^2} \exp\left(\frac{\pi^2\sigma^2}{\tau^2}\right). \tag{52}$$

With the Doppler velocity, line depth, and line width calculated, equation 49 can be used to estimate the continuum intensity.

The Fourier coefficients a_i, b_i are computed with both circular polarizations separately, and so the Doppler velocity can be computed separately as well: v_{LCP} and v_{RCP}. Then magnetic flux density along the line of sight can be computed as

$$B = (v_{\mathrm{LCP}} - v_{\mathrm{RCP}})K_m, \tag{53}$$

where $K_m = 1.0/(2.0 \times 10 \times 10^{-5}\lambda_0 g_L c) = 0.231 \mathrm{GM}^{-1}$, $g_L = 2.5$ is the Landé-g factor, and c is the speed of light.

5.3.2   Algorithm implementation

The basic input to the observables computation is a set of $N_{\mathrm{wl}} \times 2$ filtergrams, where $N_{\mathrm{wavelength}}$ is the number of wavelengths sampled, one filtergram each in LCP and RCP. The wavelength sampling is $N_{\mathrm{wl}} = 6$ in standard operation, although other sample sizes have been tested. The input filtergrams have been interpolated to a common observing time and have been co-registered, as described in previous sections. The filtergrams $I_{\mathrm{L/R},j}(\mathbf{x})$ have been ordered in increasing wavelength, so that $j = 0$ is the bluest filter position and $j = N_{\mathrm{wavelength}} - 1$ is the reddest. Once the filtergrams have been prepared in this way, the computation of the observables at each pixel is independent of any other pixel, and so for convenience we drop the image location vector $\mathbf{x}$ for the rest of this section. The nominal separation between transmission profiles is taken to be related to the narrowband Michelson free spectral range: $\delta\lambda = \mathrm{FSR}_{\mathrm{NB}}/2.5$, and so $\tau = N_{\mathrm{wl}} \cdot \mathrm{FSR}_{\mathrm{NB}}/2.5$. The HMI instrument does not measure a continuous quantity $I(\lambda)$ but instead samples the solar line at discrete points (or more precisely, convolved by distinct instrument transmission profiles; see below), so the discrete estimations of the coefficients in 47 and 48 become

$$a_{[\mathrm{L,R}],1} \approx \sum_{j=0}^{N_{\mathrm{wl}}-1} I_{[\mathrm{L,R}],j} \cos\left(2\pi\frac{2.5-j}{N_{\mathrm{wl}}}\right) \tag{54}$$

$$b_{[\mathrm{L,R}],1} \approx \sum_{j=0}^{N_{\mathrm{wl}}-1} I_{[\mathrm{L,R}],j} \sin\left(2\pi\frac{2.5-j}{N_{\mathrm{wl}}}\right) \tag{55}$$

$$a_{[\mathrm{L,R}],2} \approx \sum_{j=0}^{N_{\mathrm{wl}}-1} I_{[\mathrm{L,R}],j} \cos\left(4\pi\frac{2.5-j}{N_{\mathrm{wl}}}\right) \tag{56}$$

$$b_{[\mathrm{L,R}],2} \approx \sum_{j=0}^{N_{\mathrm{wl}}-1} I_{[\mathrm{L,R}],j} \sin\left(4\pi\frac{2.5-j}{N_{\mathrm{wl}}}\right). \tag{57}$$

Note we have neglected the leading factor of $2/\tau$ here. This factor is multiplied through later, when this factor does not cancel. Then the velocity for each polarization is com-

puted:

$$v_{\text{LCP},1} = \frac{dv}{d\lambda} \frac{(N_{\text{wl}} - 1)\text{FSR}_{\text{NB}}}{2.5} \frac{1}{2\pi} \arctan\left(\frac{-b_{\text{L},1}}{-a_{\text{L},1}}\right).$$ (58)

Note the factor of $N_{\text{wl}} - 1$ insead of N_{wl}. This is done because REASONS. The RCP velocity, $v_{\text{RCP},1}$ is computed in the same way. The velocities determined from the second Fourier coefficients are computed similarly:

$$v_{\text{LCP},2} = \frac{dv}{d\lambda} \frac{(N_{\text{wl}} - 1)\text{FSR}_{\text{NB}}}{2.5} \frac{1}{4\pi} \arctan\left(\frac{-b_{\text{L},2}}{-a_{\text{L},2}}\right).$$ (59)

The dynamic range of the second Fourier coefficients is half that of the first Fourier coefficients, so the first Fourier coefficient velocities are used to correct this:

$$v_{\text{LCPcor},2} = (v_{\text{LCP},2} - v_{\text{LCP},1} + 10.5p_{v2} \mod p_{v2}) - \frac{p_{v2}}{2} + v_{\text{LCP},1},$$ (60)

where $p_{v2} = (dv/d\lambda) \cdot (N_{\text{wl}} - 1) \cdot (\text{FSR}_{\text{NB}}/2.5)/2$. Again, the RCP velocities are computed the same way.

The validity of the above computations of velocity depend on the assumption that the transmission profiles for each I_j are delta functions, and that the solar FeI line is perfectly Gaussian. Neither assumption is valid, and so the computed Doppler velocity in, for example, equation 58, will differ systematically from the true solar Doppler velocity. A solution to this problem is take a realistic solar FeI absorption line, convolve it with the true instrument transmission profiles, and input the resulting synthetic intensities $I_{\text{s},j}$ to equations 54 – 57 to obtain the first and second Fourier coefficients, and then compute the Doppler velocities for each order coefficients. The solar line can be Doppler shifted by a range of velocities, and the measured velocity v_{coef} determined as a function of true velocity v_{sun}. Because v_{coef} turns out to be a monotonic function of v_{sun}, inverting this function is simply a matter of looking up the value of v_{sun} that corresponds to the measured v_{coef}.

The synthetic intensities are computed with the sum

$$I_{\text{s},j} = \sum_{\lambda} I_{\text{FeI}}(\lambda, \lambda_0) \cdot T(\lambda)$$ (61)

where $T(\lambda)$ is the instrument transmission profile, and $I_{\text{FeI}}(\lambda, \lambda_0$ is the same model of the FeI absorption line used in the phasemap determination (18 and 19), shifted from its rest wavelength by a Doppler shift λ_0. Because the line shape changes as a function of observing angle with respect to the solar surface, the absorption line I_{FeI} is modified as a function of distance from disk center (actually, image center). This is done by scaling the values of I_{FeI} and λ by a scaling factor that is linear in distance from disk center:

$$S(d) = \frac{c_0 + c_1 d}{c_0 + c_1},$$ (62)
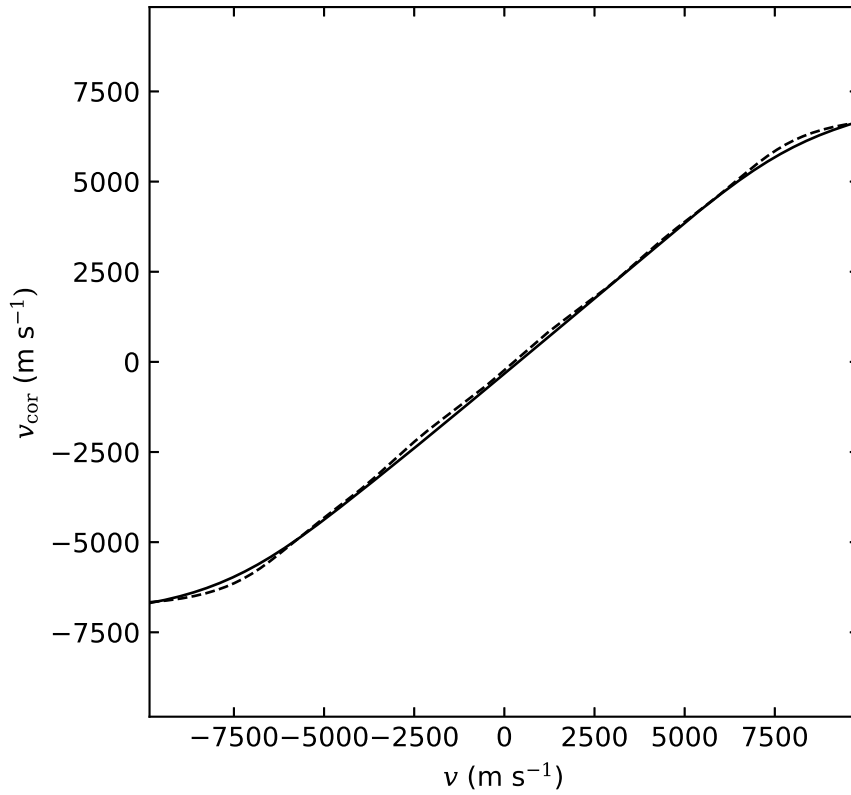
Figure 17: An example of the lookup table for velocity correction. The solid line is for the velocities computed from the first Fourier coefficients ($v_{[L,R],1}$) and the dashed line is for the velcoties computed from the second Fourier coefficients ($v_{[L,R],2}$). The lookup table shown was computed from the 2021 July 9 phasemaps (see Figure 12) and used for data processing after a retuning on 2021 July 14.

	I_g	FWHM
c_0	0.41922611	151.34559
c_1	0.24190794	-58.521771

Table 8: Coefficients for correction to line profile for observing angle. Units are in mÅ.

where d is in arc seconds and the scaling coefficients for I and λ are given in table 8. The scaled values of I_{FeI} at the scaled values of λ are then interpolated to the lookup table grid, resulting in a line that gets shallower and broader as the observing location gets closer to the limb. Note that the scaling here affects both the Voigt profile width and the contribution from the Gaussians. The lookup table is computed on a 128×128 grid. The corrected values of v are obtained by linear interpolation. For the rest of this section, all velocities used refer to these corrected values.

For the definitive observables, one final correction is applied to the velocities, to account for the slow drift of instrument tuning that occurs between updates of the lookup tables, and errors in these tables. A third order polynomial in v is subtracted from the velocities:

$$V_{\mathrm{LCP}} = v_{\mathrm{LCP}} - \left(C_0 + C_1 v_{\mathrm{LCP}} + C_2 v_{\mathrm{LCP}}^2 + C_3 v_{\mathrm{LCP}}^3 \right), \tag{63}$$

where the coefficients C_i are determined by a fit to the difference between the spacecraft velocity with respect to the Sun and the median of the calculated Doppler velocities. The velocities used to compute these coefficients are those determined in the NRT processing, which means that this polynomial correction cannot be applied to the NRT observables, and given that NRT observables are not archived, the determination of the coefficients cannot be exactly reproduced.

Now the observables can be computed. The Doppler velocity is

$$V = \frac{V_{\mathrm{LCP}} + V_{\mathrm{RCP}}}{2}. \tag{64}$$

The line-of-sight magnetic flux density is

$$B = \left(V_{\mathrm{LCP}} - V_{\mathrm{RCP}} \right) K_m. \tag{65}$$

The Fourier coefficients are now multiplied by a factor of $2/(N_{\mathrm{wl}} - 1)$. The line width is computed as

$$\sigma_{\mathrm{LCP}} = \frac{(N_{\mathrm{wl}} - 1)\mathrm{FSR}_{\mathrm{NB}}}{2.5} \frac{1}{\pi\sqrt{6}} \sqrt{\log\left(\frac{a_{\mathrm{L},1}^2 + b_{\mathrm{L},1}^2}{a_{\mathrm{L},2}^2 + b_{\mathrm{L},2}^2} \right)}, \tag{66}$$

$$\sigma = \left(\sigma_{\mathrm{LCP}} + \sigma_{\mathrm{RCP}} \right)\sqrt{\log 2}, \tag{67}$$

where $\mathrm{FSR}_{\mathrm{NB}}$ is given in Angstroms. For line depth and intensity, the computed line width σ is not used as it can take on spurious values in the presence of strong magnetic fields. Therefore the linewidth used is a fifth order polynomial in distance d (in

arcseconds) from disk center:

$$\sigma(d) = \big(100.67102 + 0.015037016d - 0.00010128197d^2 + 3.1548385 \times 10^{-7}d^3$$
$$-3.7298102 \times 10^{-10}d^4 + 1.7275788 \times 10^{-13}d^5\big) / (2000\sqrt{\log 2}), \quad (68)$$

where the coefficients were determined by fitting the measured line widths at a period of low solar activity. The line depth is then

$$I_{\text{LCP},d} = \frac{(N_{\text{wl}} - 1)\text{FSR}_{\text{NB}}}{2.5} \frac{1}{2\sqrt{\pi}\sigma(d)} \sqrt{a_{\text{L},1}^2 + b_{\text{L},1}^2} \exp\left(\pi^2\sigma(d)^2 \frac{2.5^2}{(N_{\text{wl}} - 1)^2}\right), \quad (69)$$

$$I_d = \frac{I_{\text{LCP},d} + I_{\text{RCP},d}}{2}. \quad (70)$$

Finally, the continuum intensity is estimated by

$$I_{\text{LCP},c} \approx \frac{1}{N_{\text{wl}}} \sum_{j=0}^{N_{\text{wl}}-1} \left[I_{\text{LCP},j} + I_{\text{LCP},d} \exp\left(-\frac{(2.5 - j)^2 (dv/d\lambda)^2}{\sigma(d)^2}\right)\right], \quad (71)$$

$$I_c = \frac{I_{\text{LCP},c} + I_{\text{RCP},c}}{2}. \quad (72)$$

Examples of LOS observables are shown below.
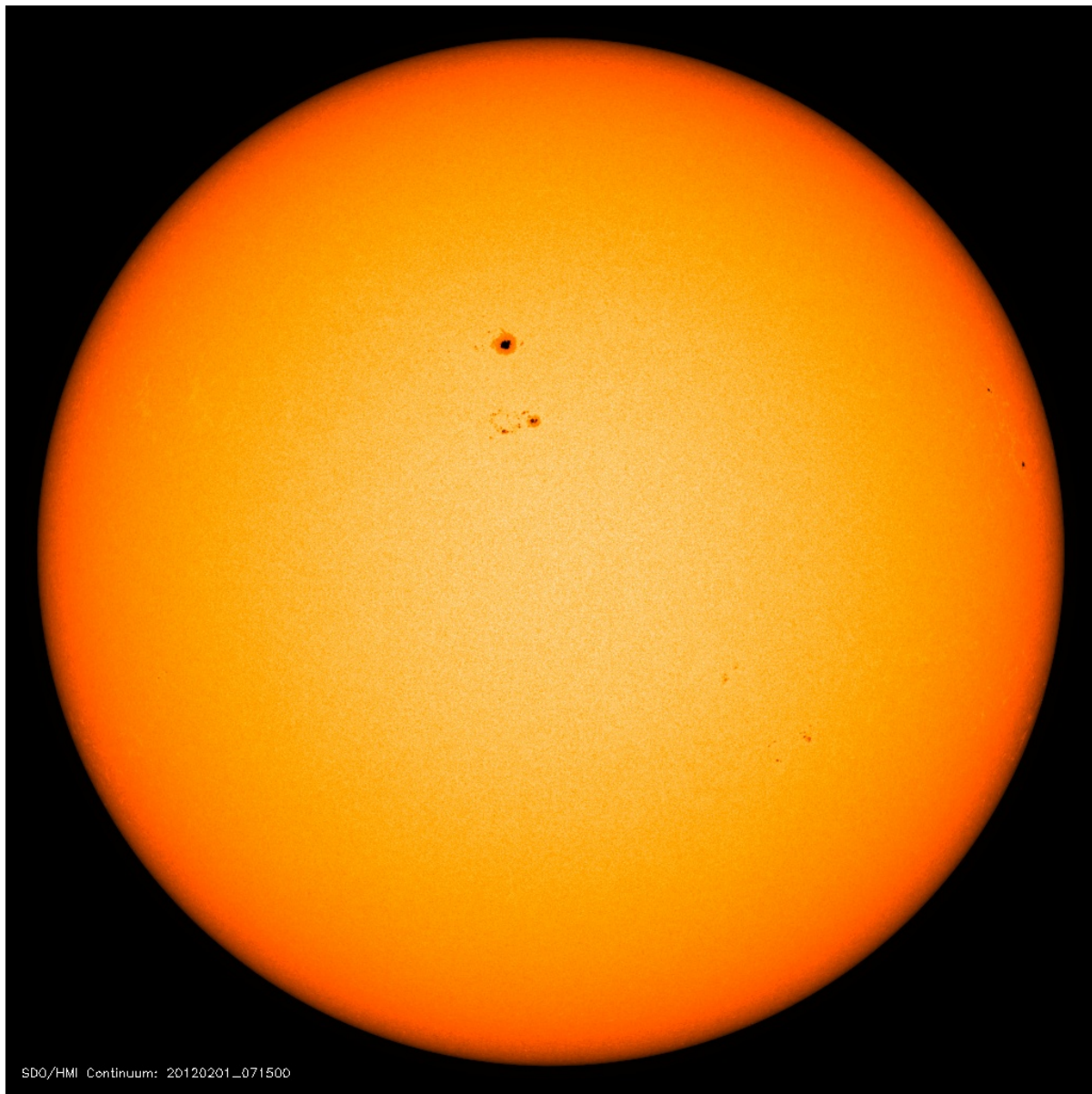
Figure 18: Continuum intensity image, estimated using the LOS observables algorithm. This image was generated for target time 2012.02.01 07:15:00_TAI.
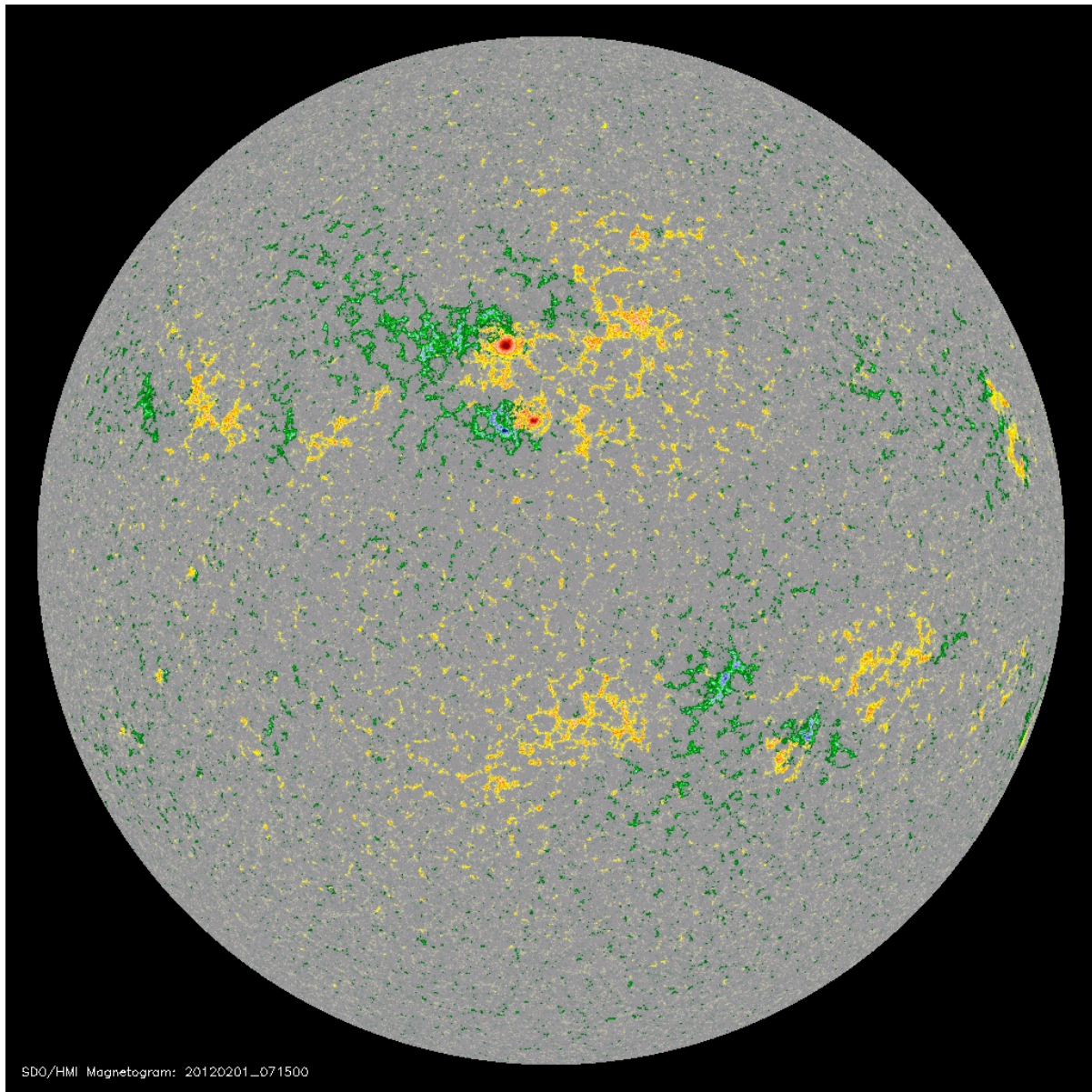
Figure 19: Line-of-sight magnetogram, showing magnetic flux density estimated by the LOS observables alogorithm. This image was generated for target time 2012.02.01 07:15:00_TAI. The color scale saturates at $\pm$ 1500 G.

Quantity	Cadence	DRMS Series Name	Noise (disk center)
Stokes I	720s	hmi.S_720s	0.05%
Stokes Q, U, V	720s	hmi.S_720s	0.09% of I
LOS Velocity	45s	hmi.V_45s	17 m s^{-1}
LOS Velocity	720s	hmi.V_720s	7 m s^{-1}
LOS Magnetic Flux Density	45s	hmi.M_45s	7 G
LOS Magnetic Flux Density	720s	hmi.M_720s	3 G
Computed Continuum Intensity	45s	hmi.Ic_45s	0.03%
Computed Continuum Intensity	720s	hmi.Ic_720s	0.01%
FeI Line Width	45s	hmi.Lw_45s	1 mÅ
FeI Line Width	720s	hmi.Lw_720s	0.4 mÅ
FeI Line Depth	45s	hmi.Ld_45s	0.05%
FeI Line Depth	720s	hmi.Ld_720s	0.02%

Table 9: Uncertainty estimates for HMI measured quantities in a single pixel at disk center (from Table 1 of S. Couvidat et al., 2016). Photon noise is 26 DN for a typical intensity of $50\,\mathrm{K\,DN}\,s^{-1}$ in a single filtergram. Higher noise of 43 DN is expected for Stokes Q, U, V, which are ten times smaller than I, even in strong-field regions.

5.4 Uncertainty Estimates in Measured Quantities

Uncertainty estimates are complex and for many scientific investigations systematic errors in the observed quantities are more important than random errors. In some sense that is a testament to the quality of the initial design and construction of the instrument. Nevertheless, estimates of random errors can be made based on photon counting statistics that are consistent with observed values on orbit. Table 9 shows the computed noise level for each of the HMI observables at disk center. The uncertainties are based on typical CCD count rates and the effects of those statistics on the determination of intensity and wavelength of the line based on the HMI algorithms. Twenty or more filtergrams contribute to each of the quantities in the table. Statistics for the Stokes parameters improved from the quoted values after a new observing sequence was initiated on 13 March 2016. See S. Couvidat et al., 2016 for more detail. The observable quantities listed here are discussed in more detail in the Volume 2 of the HMI CMADS.

A   Symbols Used

Symbols and variables used throughout this document are defined here. In many cases the notation used here matches the quoted literature, but consistency within this document is given precedence. Effort was also made to chose notation that matches variable names used in the source code for the processing software used, but this was only possible to a limited extent.

Symbol	Description
I	Vector of images with different polarization states, temperally and spatially coincident. Usually either a Stokes vector or set of HMI observed or calibrated filtergrams.
$[I, Q, U, V]$	Stokes quantities.
$[I_{\mathrm{LCP}}, I_{\mathrm{RCP}}]$	Left circularly polarized and right circularly polarized filtergrams, respectively. Equivalent to $I + V$ and $I - V$.
I_{sun}	Stokes vector of solar light that enters the instrument.
I_{HMI}	Stokes vector of light incident on the cameras. May or may not account for instrument throughput.
I_{cor}	Vector of calibrated filtergrams, corrected for the instrument's polarization characteristics.
$\mathbf{x} = (x, y)$	Position on image. Where units are relevant, usually normalized to half the image width. Where noted, units may be in arcseconds (either approximate for an average image or specific to that image) or normalized to the apparent solar radius. Often used as a generalized way to refer to indexing of image arrays.
$\mathbf{a}$	Image shift. Not to be confused with Fourrier coefficients (see below).
$F(\mathbf{x})$	Flatfield correction for gain variations in the HMI CCDs. $G(\mathbf{x}) = \log F(\mathbf{x})$. Subscripts refer to iterative determinations of the flatfield.
λ	Wavelength of light. Usually in Angstroms. The subscript 0 means the wavelength in the rest frame, or the center (maximum absorption) wavelength of the FeI line.
v	Velocity, usually of the solar surface relative to the observer (HMI/SDO). Positive velocities are velocities away from the observer (redshifted) and negative velocities are towards. Always in ms^{-1}.
V	Velocity computed from estimations of the Doppler shift in the FeI line that HMI observest. In image form, referred to as Dopplergrams. Always in ms^{-1}.
B	Magnetic flux density along the observer's line of sight, estimated from circularly polarized observations. In image form referred to as magnetograms. Always in G.
σ	Line width of the Gaussian approximation to the FeI line.
I_d	Line depth of the observed FeI line estimated from observations.

Symbol	Description
I_c	Level of the continuum intensity in models of the FeI absorption line or estimate of the continuum intensity from fits to other parameters.
a_1, b_1, a_2, b_2	First and second Fourier components, either true or estimated.
$\mathcal{O}$	Modulation matrix for the HMI instrument that transforms the input solar Stokes vector to the Stokes vector of the beam that reaches the detectors. Only accounts for polarization effects, not throughput.
$\mathcal{O}_{\mathrm{obs}}$	Modulation matrix of the HMI instrument that coverts the input solar Stokes vector into a set of observed filtergrams.
$\mathcal{D}$	Demodulation matrix — inverse of the instrument modulation matrix. Used to generate polarization-calibrated filtergrams.
$\mathcal{M}$	Mueller matrices of various instrument components. Subscripts tel, sel, and bs refer to the front window and telescope, the polarization selectors, and the polarizing beam splitter, respectively.
$T(\lambda)$	Transmission profile as a function of wavelength for a given optical element or for the HMI instrument as a whole. T is also sometimes used for temperature; the usage should be clear from context.
PSi	Polarization selector. In text this is used to refer to one of the three mechanisms, in equations it refers to the motor position relayed back in the instrument telemetry, an integer between 0 and 239.
WTi	Wavelength tuning selector. In text this is used to refer to one of the four wavelength tuning selectors, in equations it refers to the motor position relayed back in the instrument telemetry, an integer between 0 and 239.
ϕ	Angle of a movable element (polarization selector or wavelength tuning selector) with respect to the mechanism zero point.
Φ	Angle of the fast axis of a polarizing element, both fixed and movable. For rotating elements, this is the angle at the mechanism origin, and the angle of the fast axis in any given observing configuration requires knowing both Φ and ϕ.
$\mathcal{A}(\mathbf{x}, t)$	Estimate of front window fringes seen in CALMODE observations and phasemaps. Used to correct phasemaps before look-up tables are generated.
τ	Period or observing time.

B   Glossary

CALMODE	An observing mode where two lenses, one in each focus wheel, are inserted in the optical path to image the pupil on the camera. Used for calibration observations, as the name suggests, and useful because the solar light is sampled equally at every point in the image. For the other observing mode, see OBSMODE.
Dopplergram	Image of line-of-sight photospheric velocity estimated from the measured Doppler shift in the FeI line observed by HMI. See section 5.3.
DRMS	Data Record Management System – the database system in which data from the HMI and AIA instruments are stored and accessed. The DRMS consists of a relational database based on PostgreSQL and an associated data storage system (SUMS).
Filtergram	Image taken by HMI with a given wavelength tuning and polarization selected. Can refer to the raw images taken by the instrument (level 0 for completely uncorrected, level 1 if basic image corrections like flatfields and dark current subtraction have been applied), or to calibrated images in Stokes I, Q, U, V or circularly polarized images $I + V, I - V$, or to calibration images.
Framelist	A sequence of filtergrams taken at a set cadence and period. All nominal science data and calibration observations are taken with pre-defined framelists. See appendix C.1.
JSOC	The Joint Science and Operations Center – the facilities for the operation of the HMI and AIA instruments and the processing and distrubution of their data. The facilities are hosted and staffed by Stanford University and Lockheed Martin Solar & Astrophysics Laboratory. Consists of the Instrument Operations Center (JSOC-IOC) which is responsible for monitoring and commanding the two instruments, and the Science Data Processing center (JSOC-SDP) which captures, processes, distrubutes, and stores all instrument data and science data products.
Magnetogram	Image of the line-of-sight magnetic flux density at the photosphere estimated from the circularly polarized filtergrams taken by HMI. See section 5.3.
Mod C	Standard six wavelength position observing sequence. The front camera (camera 2) takes circuluarly polarized filtergrams and is used for LOS observables; the side camera (camera 1) takes both linearly and circularly polarized fitlergrams, and is used for vector data products. Used until 2016 April 13.

Mod L	Standard six wavelength position observing sequence. The front camera (camera 2) takes circularly polarized filtergrams while the side camera (camera 1) takes only linearly polarized filtergrams. LOS observables are calculated from front camera images, vector products combine images from both cameras. Used from 2016 April 13 onwards.
NRT	Near Real Time data, also called quicklook data. Products produced with as short a time lag as possible for users who need solar observations as close to real-time as is feasible. In general fewer calibrations are applied and error statistics are worse than the definitive data that take longer (often several days) to produce. These data are not archived.
Observables	Scalar line-of-sight quantities (velocity, magnetic field flux density, continuum intensity, etc.) that are computed as part of HMI's standard scientific data product suite and can be calibrated in physical units.
OBSMODE	The standard observing mode where the instrument is in focus. See CALMODE for the alternative observing mode.
Phasemaps	Determination of the relative phases of the seven elements in the filter section with polarizers. Used to determine how best to co-tune the instrument and to compute the transmission profiles. See section 4.8.
SUMS	Storage Unit Management System – the data storage system that handles the storage of data associated with records in the DRMS.

C   HMI Standard, Calibration, and Special Observing Sequences

Almost all images taken by the HMI instrument are taken automatically, controlled by the instrument's sequencer. The sequencer controls the selection of focus, wavelength tuning, polarization, exposure time, and camera. A sequence of images executed once or repeatedly is referred to as a framelist, which comprises one or more image commands over a defined period of time. Most framelists used on orbit have an execution time of either 90 seconds or 135 seconds. This is referred to as the framelist cadence, which is distinct from the image cadence (typically 1.875 seconds). The sequencer can only execute one framelist at a time, and unless an error is encountered will always complete the entire framelist before beginning another. A Framelist Timeline Specification (FTS) selects the timing, frequency, and repetition count of a framelist, referenced to the start of each day. Each FTS has a unique four digit ID. Some FTS IDs command their framelist to be executed continuously (the standard observing sequences behave this way) while others command only intermittent executions of their framelist (for example, the daily calibration sequences that execute twice per day at 06:00 UT and 18:00 UT). A priority system allows multiple FTS IDs to be active at once, with lower priority FTS IDs selecting the executed framelist where higher priority FTS IDs have gaps.

Most high level science products do not identify which sequences were being run, but level 0 and level 1 filtergrams identify the FTS ID with the keyword HFTSACID (see appendix E). The framelist itself is not identified in any metadata or housekeeping telemetry, and needs to be referenced from the FTS ID. A list of all current FTS IDs loaded on the instrument is available on the JSOC webpage (`http://jsoc.stanford.edu/doc/data/hmi/FTSID_v05.txt`). This appendix describes many of the most commonly used framelists and FTS IDs.

C.1   Framelists

The most commonly used framelists are listed in Table 12. For the first six years of operations, the front camera took circular polarization states only, and was used to generate all line-of-sight 45 second cadence data products (in particular Dopplergrams and LOS magnetograms), while the side camera took all polarization states, and was used for vector field inversion products. The front camera would take filtergrams in all six wavelength tunings in both LCP and RCP every 45 seconds. The side camera, with four additional polarization states to sample, completed its sequence every 135 seconds. This observing scheme was known to the instrument team as mod C. The redundant observations on both cameras of the circular polarization states could be avoided if filtergrams from both cameras were combined in the vector field inversions, and this observing scheme, known internally as mod L, was adopted on 2016 April 13.

Name	Cadence	Description
Standard observing framelists		
obs_6Cv01	135s	Standard observing sequence with circular polarization taken on the front camera, all polarizations taken on the side camera. Known as mod C. All line-of-sight products use front camera filtergrams, all vector products use side camera filtergrams.
obs_6Cv02	135s	Same filtergram sequence as obs_6Cv01. Changes allow more convenient updating of instrument settings but do not affect the data.
obs_6Lv02	90s	Standard observing sequence with circular polarization taken on the front camera, linear polarization taken on the side camera. Known as mod L. All line-of-sight products use front camera filtergrams, all vector products use filtergrams from both cameras.
Daily calibration framelists		
cal_6Cv01	135s	Daily calibration observations. Includes dark frames, CALMODE images, and continuum-tuned filtergrams.
cal_6Cv02	135s	Same as the above framelist.
cal_6Lv02	90s	Same calibration frames as the mod C version, but in a 90s framelist.
Flatfield framelists		
pzt_cal_6Cv02	135s	Framelist for flatfield determination using the ISS mirror to off-center the solar disk. Taken in CALMODE.
pzt_def_6Cv02	135s	Framelist for flatfield determination using the ISS mirror to off-center the solar disk. Taken in standard focus.
pzt_cal_6Lv02	90s	Same as pzt_cal_6Cv02 but in a 90s framelist.
pzt_def_6Lv02	90s	Same as pzt_def_6Cv02 but in a 90s framelist.
focus_off_v01	45s	Sequence of filtergrams at single wavelength and polarization, different focus settings. The default focus setting is taken twice. One dark per camera is also taken. Used during flatfield off-point maneuvers.
focus_off_v02	45s	Same as the above framelist.
Detune framelists		
det_cal_6Cv01	135s	Detune sequence taken in CALMODE.
det_cal_6Cv02	135s	Same as the above framelist.
det_def_6Cv01	135s	Detune sequence taken in normal focus.
det_def_6Cv02	135s	Same as the above framelist.
Focus sweep framelists		
focus_6Cv01	135s	Full focus sweep in a 135s second framelist
focus_6Cv02	135s	Same as the above framelist.

Name	Cadence	Description
focus_6Lv02	90s	Same as the Mod C full focus sweep, but in a 90s framelist.
focr_6Cv01	135s	Reduced focus sweep, with only 7 focus positions centered around focus position 11.
focr_6Cv02	135s	Same as the above framelist.
focr_6Cv03	135s	Same as above framelists, but centered around focus position 10.
focr_6Lv02	90s	Same as equivalent mod C framelist, but in a 90s framelist.
focr_6Lv03	90s	Same as equivalent mod C framelist, but in a 90s framelist.
Other calibration framelists		
calmode_6L	90s	Standard Mod L observing sequence, but taken with the instrument in CALMODE.
lin_cal_6Cv01	135s	Calibration sequence to measure CCD linearity. Takes a series of filtergrams with increasing exposure time. Also takes dark frames. All frames taken in CALMODE.
lin_cal_6Cv02	135s	Same as above framelist.
lin_def_6Cv01	135s	Same as above framelists, but taken in default focus setting.
Maneuver and special observation framelists		
comet_ison	135s	Framelist for comet observations. Images are 320ms exposures at 2.25s cadence, taken in a single polarization and wavelength tuning.
cruc_offp_lin	135s	Test of long exposures used during offpoint maneuver. Images are taken at half the normal cadence.
loop_led_45	45s	LED exposures used during offpoint maneuvers.
merc_1pl_v01	45s	Framelist for transits of Mercury. Front camera takes normal Mod C/Mod L sequence, side camera takes continuum-tuned images in a single linear polarization state.
regulus_135	135s	Framelist for spacecraft pointing at star Regulus. Contains a mix of standard and long (3.2s) exposures, as well as dark frames. Images taken at half the normal cadence.
regulus_long	135s	Same as the above framelist but only uses long (3.2s) exposures.
roll_dop_ic2	45s	Standard observing sequence on front camera, continuum-tuned filtergrams on the side camera. Run during roll maneuvers.
rolldopic_v02	45s	Same as above framelist.
rolldopic_v03	45s	Same as above framelists.

Name	Cadence	Description
rollicscn_v01	45s	Same as above framelists.
venus_2pl_v01	135s	Framelist for transit of Venus. Front camera takes normal Mod C sequence, side camera takes continuum-tuned images in two linear polarization states.
venus_4pl_v01	135s	Same as above framelist but side camera takes four linear polarization states.

Table 12: Framelists used during the prime and extended missions. Framelists used only during ground testing and on-orbit commissioning are not included. Note that the same image sequence can be implemented in different ways, leading to different framelists with identical data. The differences are not relevant to data analysis, but all framelists used are included here for completeness.

C.2   Framelist Timeline Specifications

The framelist Timeline Specification (FTS) IDs used during the prime and extended missions are listed here. Some FTS IDs run continuously (such as the standard observing sequences) until interrupted by a higher priority FTS ID, while others only take observations at periodic intervals (for example, the daily calibrations sequences that execute once every twelve hours).

FTS ID	Framelist	Cad.	Repetition	Description
Standard observing sequences				
1021	obs_6Cv02	135s	continuous	Standard Mod C observing sequence.
1022	obs_6Lv02	90s	continuous	Standard Mod L observing sequence.
Calibration sequences				
2001	cal_6Cv01	135s	periodic	Daily calibration sequence (Mod C).
2002	focr_6Cv01	135s	periodic	Reduced focus sweeps repeated every twelve hours. Used for cross-calibration observations with SoHO/MDI.
2004	focr_6Cv01	135s	periodic	Reduced focus sweeps repeated every 144 minutes. Used for cross-calibration observations with SoHO/MDI.

FTS ID	Framelist	Cad.	Repetition	Description
2021	cal_6Cv02	135s	periodic	Daily calibration sequence (Mod C).
2025	focr_6Cv02	135s	periodic	Reduced focus sweeps repeated every 90 minutes. Used to assess focus variation throughout the day.
2042	cal_6Lv02	90s	periodic	Daily calibration sequence (Mod L).
2043	cal_6Lv02	90s	periodic	Daily calibration sequence (Mod L), repeated hourly.
3000	focr_6Cv01	135s	continuous	Reduced focus sweep for weekly calibrations.
3001	pzt_def_6Cv01	135s	continuous	PZT flatfield sequence in standard focus, Mod C.
3002	pzt_cal_6Cv01	135s	continuous	PZT flatfield sequence in CALMODE, Mod C.
3003	focus_6Cv01	135s	continuous	Full focus sweep, Mod C.
3004	lin_def_6Cv01	135s	continuous	CCD linearity calibration sequence, normal focus.
3005	lin_cal_6Cv01	135s	continuous	CCD linearity calibration sequence, CALMODE.
3006	det_def_6Cv01	135s	continuous	Detune sequence, normal focus.
3007	det_cal_6Cv01	135s	continuous	Detune sequence, CALMODE.
3008	focus_6Cv01	135s	periodic	Full focus sweeps repeated every 9 minutes, used for eclipse recovery monitoring.
3010	focr_6Cv01	135s	periodic	Reduced focus sweeps, repeated every 22.5 minutes. Used to monitor recovery from lunar transits.
3012	focr_6Cv01	135s	periodic	Reduced focus sweeps repeated every 45 minutes, used for eclipse recovery monitoring.
3020	focr_6Cv02	135s	continuous	Reduced focus sweep for weekly calibrations.
3021	pzt_def_6Cv02	135s	continuous	PZT flatfield sequence in standard focus, Mod C.
3022	pzt_cal_6Cv02	135s	continuous	PZT flatfield sequence in CALMODE, Mod C.
3023	focus_6Cv02	135s	continuous	Full focus sweep for weekly calibrations.
3026	det_def_6Cv02	135s	continuous	Detune sequence, normal focus.
3027	det_cal_6Cv02	135s	continuous	Detune sequence, CALMODE.

FTS ID	Framelist	Cad.	Repetition	Description
3028	focus_6Cv02	135s	periodic	Full focus sweeps repeated every 9 minutes, used for eclipse recovery monitoring.
3031	focr_6Cv02	135s	periodic	Reduced focus sweeps repeated every 33.75 minutes, used for eclipse recovery monitoring.
3032	focr_6Cv02	135s	periodic	Reduced focus sweeps repeated every 45 minutes, used for eclipse recovery monitoring.
3034	lin_cal_6Cv02	135s	periodic	CCD linearity calibration sequence taken in CALMODE, repeated every 90 minutes.
3035	det_cal_6Cv02	135s	periodic	Periodic CALMODE detunes every 72 minutes.
3036	det_cal_6Cv02	135s	periodic	Periodic CALMODE detunes every 90 minutes.
3040	focr_6Lv02	90s	continuous	Reduced focus sweep (focus 11) used for weekly calibrations (Mod L).
3041	pzt_def_6Lv02	90s	continuous	PZT flatfield sequence in standard focus, Mod L.
3042	pzt_cal_6Lv02	90s	continuous	PZT flatfield sequence in CALMODE, Mod L.
3043	focus_6Lv02	90s	continuous	Full focus sweeps for weekly calibrations (Mod L).
3044	focr_6Lv03	90s	continuous	Reduced focus sweep (focus 10) used for weekly calibrations (Mod L).
3048	cal_6Lv02	90s	continuous	Mod L calibration sequence run continuously. Used to test the framelist.
3076	det_def_6Cv02	135s	periodic	Detune sequence in standard focus, repeated every 238.5 minutes (4 hours).
3077	det_cal_6Cv02	135s	periodic	Detune sequence in CALMODE, repeated every 238.5 minutes (4 hours).
3086	det_def_6Cv02	135s	periodic	Detune sequence in standard focus, repeated every three hours.
3087	det_cal_6Cv02	135s	periodic	Detune sequence in CALMODE, repeated every three hours.

FTS ID	Framelist	Cad.	Repetition	Description
3128	focus_6Lv02	90s	periodic	Full focus sweeps repeated every nine minutes, used for eclipse recovery monitoring (Mod L).
3132	focr_6Lv02	90s	periodic	Reduced focus sweeps (focus 11) repeated every 45 minutes, used for eclipse recovery monitoring (Mod L).
3135	focr_6Lv03	90s	periodic	Reduced focus sweeps (focus 10) repeated every 45 minutes, used for eclipse recovery monitoring (Mod L).
Special observing and calibration framelists				
4010	loop_led_45	45s	continuous	LED exposure sequence.
4011	focus_off_v02	45s	continuous	Offpoint flatfield sequence.
4012	regulus_135	135s	continuous	Sequence for observation of Regulus.
4013	roll_dop_ic2	45s	continuous	Sequence for roll maneuvers.
4014	cruc_offp_lin	135s	continuous	Long exposure test sequence.
4015	regulus_long	135s	continuous	Sequence for observation of Regulus.
4031	focus_off_v02	45s	continuous	Offpoint flatfield sequence.
4033	rolldopic_v02	45s	continuous	Sequence for roll maneuvers.
4034	venus_2pl_v01	135s	continuous	Venus transit observing sequence, with 2 linear polarization states.
4035	venus_4pl_v01	135s	continuous	Venus transit observing sequence, with 4 linear polarization states.
4036	comet_ison	135s	continuous	Comet offpoint observing sequence.
4037	rolldopic_v03	45s	continuous	Sequence for roll maneuvers.
4038	rollicscn_v01	45s	continuous	Sequence for roll maneuvers.
4039	merc_1pl_v01	45s	continuous	Mercury transit observing sequence, with 1 linear polarization state.
4041	calmode_6L	90s	periodic	Standard observing sequence taken in CALMODE, repeated once per hour.

Table 13:

D　Filtergram and Sequencer Settings

The characteristics of a given filtergram — its wavelength coverage or polarization measurement, for example — depend on the configuration of the optics package at the time the observation is made and the camera that records the image. This section describes the configuration states of the instrument, how these states are recorded and encoded in the metadata, and how desired filtergram types can be identified.

D.1　Filtergram ID

Every filtergram taken as part of an observing sequence is identified by an ID number, the Filtergram ID or FID, that can in most cases be used to identify the important parameters of that filtergram. This includes the wavelength tuning, polarization selection, or calibration image type. It must be noted, however, that no consistency in FIDs is enforced. Multiple FIDs can refer to the exact same filtergram parameters, which filtergrams with the same FID can be taken with different instrument configurations. In the normal observing modes, however, FIDs can be used to identify filtergram parameters without issue.

For standard science observations, each filtergram has a five-digit FID. The leading two digits are constant, the following two (10^2 and 10^1) identify the wavelength tuning, and the lowest order digit identifies the polarization selection. Table 14 lists these FID combinations. The polarization and wavelength IDs in Table 14 are explained below in sections D.2 and D.3, respectively.

D.2　Polarization Selection IDs

There are three polarization selectors in the HMI optics package. Two are sufficient to select any linear or circular polarization state; the third is for redundancy. Framelists (see appendix C.1) specify the polarization setting for each exposure using a polarization ID, which references an oboard table with motor positions for each polarization selector. We do not include the entire list here, but the ten polarization IDs used for almost all images during on-orbit operations are shown in table 15. The first four PL IDs shown are for the mod A observing sequence that was never used for science observations. The IDs 414 – 417 are linear polarization states. In the current observing campaign they are taken only by camera 1. The final two, 418 and 419, are circularly polarized, and are taken on camera 2. For filtergrams taken by some framelists the polarization state is unimportant, and specifies DEFAULT, which is determined by the sequencer settings. For the sequencer in normal configuration, the default is 410. The settings in table 15 have not been changed since the begining of the prime mission.

FID	PL Index	Polarization selection
10**0	410	Mod A pol 1
10**1	411	Mod A pol 2
10**2	412	Mod A pol 3
10**3	413	Mod A pol 4
10**4	414	$I + Q$, linear polarization, $0°$
10**5	415	$I - Q$, linear polarization, $90°$
10**6	416	$I + U$, linear polarization, $45°$
10**7	417	$I - U$, linear polarization, $135°$
10**8	418	$I + V$, left circular polarization
10**9	419	$I - V$, right circular polarlization
FID	**WL Index**	**Wavelength offset**
1000*	0xff00	-344.0 mÅ
1001*	0xff01	-309.6 mÅ
1002*	0xff02	-275.2 mÅ
1003*	0xff03	-240.8 mÅ
1004*	0xff04	-206.4 mÅ
1005*	0xff05	-172.0 mÅ
1006*	0xff06	-137.6 mÅ
1007*	0xff07	-103.2 mÅ
1008*	0xff08	-68.8 mÅ
1009*	0xff09	-34.4 mÅ
1010*	0xff0a	0.0 mÅ
1011*	0xff0b	34.4 mÅ
1012*	0xff0c	68.8 mÅ
1013*	0xff0d	103.2 mÅ
1014*	0xff0e	137.6 mÅ
1015*	0xff0f	172.0 mÅ
1016*	0xff10	206.4 mÅ
1017*	0xff11	240.8 mÅ
1018*	0xff12	275.2 mÅ
1019*	0xff13	309.6 mÅ

Table 14: Identification of polarization selection and wavelength tuning from standard framelist FIDs.

PL ID	PS1	PS2	PS3	Polarization selection
410	75	53	34	Mod A pol 1
411	75	53	52	Mod A pol 2
412	60	53	82	Mod A pol 3
413	60	53	64	Mod A pol 4
414	75	53	28	$I + Q$, linear polarization, $0°$
415	75	53	58	$I - Q$, linear polarization, $90°$
416	60	53	88	$I + U$, linear polarization, $45°$
417	60	53	58	$I - U$, linear polarization, $135°$
418	69	53	43	$I + V$, left circular polarization
419	69	53	73	$I - V$, right circular polarlization

Table 15: Most commonly used polarization selection IDs. See section 4.9 for a discussion of the meaning of the motor positions.

D.3   Wavelength Tuning IDs

The HMI filter section can be co-tuned to twenty different positions, with a nominal spacing of 34.4mÅbetween adjacent tunings. Unlike the polarization settings, the motor positions that most closely co-tune the three tunable elements change slowly with time, and so these settings, called the tuning, need to be updated periodically. In order to avoid having to re-write and re-load every single framelist on the instrument every time the instrument is retuned, the wavelength IDs in every framelist do not refer to specific motor positions, but instead to a table with motor positions that can be updated. On the instrument, the position in this table is identified by an index called the Wavelength Tuning Set Index. This index is included in the keywords for every level 0 and level 1 record. The co-tuning motor positions are given in table 16.

D.4   Focus Setting

Coarse focus control is maintained by two focus wheels which can move various combinations of glass blocks of various thicknesses in or out of the optical path. The focus settings are identified by an index from 1 to 16, each of which corresponds to a pair of focus wheel positions. There is a further focus setting, index 17, that places a lense in the optical path that images the entrance pupil. This configuration is refered to as CALMODE. The focus setting can be specified in a framelist, or left to the sequencer default setting. Focus setting 11 was the default from commissioning until 2018 October 16. The default was afterwards changed to setting 10. The configuration of the two focus wheels for each focus index is given in table 17.

WL ID	ΔWT1	ΔWT2	ΔWT4	$\Delta\lambda$
0xff00	-30	0	0	-344.0 mÅ
0xff01	-27	-6	-12	-309.6 mÅ
0xff02	-24	-12	-24	-275.2 mÅ
0xff03	-21	-18	24	-240.8 mÅ
0xff04	-18	-24	12	-206.4 mÅ
0xff05	-15	-30	0	-172.0 mÅ
0xff06	-12	24	-12	-137.6 mÅ
0xff07	-9	18	-24	-103.2 mÅ
0xff08	-6	12	24	-68.8 mÅ
0xff09	-3	6	12	-34.4 mÅ
0xff0a	0	0	0	0.0 mÅ
0xff0b	3	-6	-12	34.4 mÅ
0xff0c	6	-12	-24	68.8 mÅ
0xff0d	9	-18	24	103.2 mÅ
0xff0e	12	-24	12	137.6 mÅ
0xff0f	15	-30	0	172.0 mÅ
0xff10	18	24	-12	206.4 mÅ
0xff11	21	18	-24	240.8 mÅ
0xff12	24	12	24	275.2 mÅ
0xff13	27	6	12	309.6 mÅ

Table 16: Relative motor positions for the twenty co-tunings available. A wavelength tuning index specifies motor positions for the co-tuning at the center of HMI's spectral coverage, and the other tuning positions can be obtained relative to these positions. The relative wavelength positions are the nominal spacings as designed. The actual throughput maxima are determined as discussed in section 4.8.

Focus Ind	CF1	CF2	element 1	element 2	Notes
1	28	31	BLANK	BLANK	
2	28	103	BLANK	0.85 mm	
3	28	139	BLANK	1.7 mm	
4	28	175	BLANK	2.55 mm	
5	100	31	3.4 mm	BLANK	
6	100	103	3.4 mm	0.85 mm	
7	100	139	3.4 mm	1.7 mm	
8	100	175	3.4 mm	2.55 mm	
9	172	31	6.8 mm	BLANK	Nom. focus (before 2018.10.16)
10	172	103	6.8 mm	0.85 mm	Nom. focus (after 2018.10.16)
11	172	139	6.8 mm	1.7 mm	
12	172	175	6.8 mm	2.55 mm	
13	64	31	10.2 mm	BLANK	
14	64	103	10.2 mm	0.85 mm	
15	64	139	10.2 mm	1.7 mm	
16	64	175	10.2 mm	2.55	
17	136	67	6.8mm lens	5mm lens	CALMODE

Table 17: Focus settings parameters. The focus index is used by command or by framelist to set the focus of the instrument. The focus wheels are moved to the associated positions CF1 and CF2. The parameters of the elements placed in the elements are give as element 1 and 2, respectively.

Exp ID	τ_{exp}	Exp ID	τ_{exp}	Exp ID	τ_{exp}	Exp ID	τ_{exp}	Exp ID	τ_{exp}
1	40	11	125	21	175	31	300	41	1400
2	50	12	130	22	180	32	320	42	1600
3	60	13	135	23	185	33	340	43	1800
4	70	14	140	24	190	34	360	44	2000
5	80	15	145	25	195	35	380	45	2200
6	90	16	150	26	200	36	400	46	2400
7	100	17	155	27	220	37	600	47	2600
8	110	18	160	28	240	38	800	48	2800
9	115	19	165	29	260	39	1000	49	3000
10	120	20	170	30	280	40	1200	50	3200

Table 18: Exposure time index table. All exposure times are given in milliseconds. These values can be applied to either camera.

D.5 Exposure Time

The commanded exposure time for each camera can be set explicitly in a framelist, or left to the default setting. The default setting is specific to each camera, and is specified by referencing an index in a table. The settings are given in table 18.

D.6 Camera Readout Settings

The two cameras can each be configured in a number of ways for flexibility and redundancy. Some of these settings are included in level 0 and level 1 keywords.

E   Metadata for Filtergrams and Data Products

Every filtergram, image, data segment, data cube, or table from an HMI observation or data product has a set of associated metadata that identifies what the data are and how they were generated. These metadata are necessary for any analysis of HMI data. Within the JSOC-SDP system, the metadata are stored as keywords in a database known as the Data Record Management System (DRMS), described further in Appendix F. When exported to external users, the metadata may be disseminated as keywords in a FITS header or as a JSON object or in some other format. In this section, we will use the terminology of the DRMS: the metadata are keywords, each class of data product (for example, the set of level 1 filtergrams) is a data series, and the individual elements of that data product (one specific filtergram in the level 1 filtergrams data series, for example) is a data record. The data themselves are referred to as segments (a level 1 filtergram record contains two segments — the image itself, and an array of bad pixels and cosmic ray hits). Keywords are associated with records rather than segments, and every record in a series has the same set of keywords.

In this appendix we describe most keywords found in level 0, level 1, and level 1.5 data series. They are grouped by type and by source, rather than by series, as many keywords can be found in multiple different series. Keywords have a number of different sources: they can be read from instrument or spacecraft telemetry, they can be generated from external data products (like spacecraft ephemeris), they can be computed from the data segments themselves, or they can be inherited from other records. We give a brief definition of each keyword, identify its source, and reference the section of this document where more information can be found, if applicable.

E.1   Data Sources

Level 0 records are generated from two input sources: the high-rate telemetry packets that contain the data from the CCDs themselves and limited metadata, and the Image Status Packet (ISP) associated with a given image, which contains telemetry describing the state of the instrument sequencer and cameras when the image was taken. Both of these packets are transmitted over the dedicated high-rate connections between the JSOC-SDP and the ground stations at White Sands. Level 1 records take level 1 records as inputs but include information from a number of further sources. Calibration data, such as dark current images and flat fields, are described in the main text. Information about the spacecraft status, in particular the Attitude Control System (ACS) configuration and spacecraft pointing, are read in from the Ancillary Science Data (ASD) packet, which is provided at a lower cadence than the image cadence (normally every 4 seconds). Spacecraft ephemeris — position and velocity — are provided by the mission Flight Dynamics System (FDS), and these are interpolated to provide position metadata for each level 1 record. Information about the relative orientation between the HMI image plane and the spacecraft are provided in the Master Pointing Table (MPT) which is updated

weekly. The image position keywords are estimated from the previous month's worth of filtergrams in the most blue-ward tuning used in the standard observing sequence. Camera 1 uses the $I + U$ polarization, and camera 2 uses the $I - V$ polarization. Image rotation and scale are fixed. The former was determined from pre-launch calibrations and updated once on-orbit after recalibration using planetary transits. Level 1.5 records include a number of calibration inputs, described in the main text. In addition, temperature information is included in the metadata, derived from the housekeeping telemetry captured separately from the high-rate data streams. These data are collected once per day and so are not available for NRT data products.

Keyword	Description	Reference
General keywords. Set by the processing modules for every record.		
BLD_VERS	Build Version: which version of the JSOC pipeline software was used to generate the record.	
ORIGIN	Origin of the data record — JSOC/SDP for all official HMI data products.	
DATE	Date and time that the data record was produced	
TELESCOP	Telescope and instrument of origin — always SDO/HMI.	
Time and camera keywords (level 0 and 1).		
T_OBS	The mid-point of the observation time. Computed as the average of the open and close time sensed by three photodiodes on the shutter assembly. These are telemetry points included in the ISP.	
FSN	Filtergram Sequence Number — the HMI sequencer increments this counter by one for every image taken. Uniquely identifies each filtergram taken.	
DATE__OBS	The start-point of the observation time. In practice, calcuted as T_OBS - EXPTIME/2	
EXPTIME	Mean shutter open time. Three photodiodes sense the begining and end of illumination. The average of the three differences is the exposure time.	
EXPSDEV	The standard deviation of the three measures of exposure time.	
INSTRUME WAVELNTH WAVEUNIT	Can be either HMI_FRONT2 or HMI_SIDE1	
CAMERA	Identifies which camera the image was taken with. Camera 1 is the side camera, camera 2 is front camera. LOS observables use data from camera 2.	
IMG_TYPE	LIGHT or DARK. Set DARK if EXPTIME = 0.	

Keyword	Description	Reference
FID	Filtergram ID number — identifies the wavelength tuning, polarization setting, and sometimes other settings.	App D.1
Quality and calibration keywords. Described in E.2 and E.3.		
QUALITY	This keyword is zero for records with no known issues or defects. Non-zero quality bits are described below.	App E.2
QUALLEV0	Keyword with the level 0 quality in the associated level 1 record.	App E.2
QUALLEV1	Keyword with the quality bits for the level 1 records used in the given level 1.5 record.	App E.2
CALVER32	Calibration version (32 bit)	App E.3
CALVER64	Calibration version (64 bit)	App E.3
World Coordinate System (WCS) keywords.[2].		
WCSNAME	The WCS system name.	
CTYPEi	The WCS coordinate system type. Is HPLN-TAN (SOLARX) and HPLN-TAN (SOLARY) for HMI filtergrams and observables.	
CUNITi	The units of the axis. For filtergrams and observables this is arcseconds.	
CRVALi	The coordinate value of the axis origin. Usually 0.	
CDELTi	The coordinate scale. For filtergrams and observables, this is the same as the plate scale. For level 1 this is calculated by the limb finder. For level 1.5 this is chosen by the processing module.	Sec 5.2.2.1, 5.2.2.2
CRPIXi	The position of the coordinate origin. For filtergrams and observables, the origin is the center of the solar disk. For level 1 this is calculated by the limb finder. For level 1.5 this is chosen by the processing module. Note that these values are 1-indexed, not 0-indexed.	Sec 5.2.2.1, 5.2.2.2
CROTA2	Rotation angle of image with respect to the coordinate system. The angle of the solar north axis with respect to the image vertical. Computed from the spacecraft pointing information (FDS) and the instrument rotation (MPT).	
CRDERi	Estimate of the random error in the cooridinate.	
CSYSERi	Estimate of the systematic error in the coordinate.	
Image statistics keywords.		

---

[2]See FITS standard, `https://fits.gsfc.nasa.gov/fits_standard.html`

Keyword	Description	Reference
TOTVALS	Total pixels in the data segment image. For level 0 and 1 records, this is the total number of pixels in the valid image area but does not count pixels outside the crop radius. For level 1.5 images this is the total number of points at which observable quantities were estimated.	
DATAVALS	Total number of pixels with valid data values. For level 0 and 1 records this the count of pixels successfully decoded. For level 1.5 records this is TOVALS - MISSVALS.	
MISSVALS	Number of missing values. For level 0 and 1 this is TOTVALS - DATAVALS. For Level 1.5 this is the number of pixels in the image where the observables algorithm failed to find valid values.	
PERCENTD	Percentage of total expected pixels that are valid values.	
DATAMIN	Minimum data value. For level 0 and 1 records this is over every valid pixel decoded from the telemetry packets. For level 1.5 records this is for all valid pixel values within 0.99RSUN_OBS of disk center.	
DATAMAX	Maximum data value. Same domain as DATAMIN	
DATAMEDN	Median data value. Same domain as DATAMIN	
DATAMEAN	Mean of all data values. Same domain as DATAMIN	
DATARMS	Root mean square deviation of all data values from DATAMEAN. Same domain as DATAMIN	
DATASKEW	Skewness of the distribution of data values. Same domain as DATAMIN	
DATAKURT	Kurtosis of the distribution of data values. Same domain as DATAMIN	
DATAMIN2	Minimum value of all valid pixels (only level 1.5)	
DATAMAX2	Maximum value of all valid pixels (only level 1.5)	
DATAMED2	Median value of all valid pixels (only level 1.5)	
DATAMEA2	Mean value of all valid pixels (only level 1.5)	
DATARMS2	Root mean square deviation of all valid pixels from DATAMEA2 (only level 1.5)	
DATASKE2	Skewness of the distribution of valid data values (only level 1.5)	
DATAKUR2	Kurtosis of the distribution of valid data values (only level 1.5)	

Keyword	Description	Reference
RAWMEDN	Median of the uncorrected Doppler velocities (before the polynomial correction 63 is applied). Only for the level 1.5 Dopplergram series	Sec 5.3.2, eq 63
Level 0 keywords from high rate telemetry packets.		
TLMDSNAM	Telemety data series name with first packet of the image.	
IMGFPT	Time stamp of the first image packet.	
IMGAPID	Image Application ID	
TAPCODE	Take A Picture code — the readout mode of the camera.	
BITSELID	Bit Select ID — r value for the data compression.	
COMPID	Image compression N and K	
CROPID	ID for the crop table — pixels far enough off the solar limb are cropped from the image to save bandwidth.	
LUTID	Look-up table ID — table used on board to compress the data range. Should not be confused with the look-up tables used for observables processing.	
NPACKETS	Number of packets from which the image was constructed.	
NERRORS	Number of decompression errors in the image	
EOIERROR	End Of Image Error — last pixel error occurred in the image.	
HEADRERR	Header error occurred in the image.	
OVERFLOW	Data overflow error occurred in the image.	
Image Status Packet (ISP) keywords.		
ISPSNAME	Image Status Packet Series Name — the name of the data series that contains the ISP for this record.	
ISPPKTIM	Image Status Packet Time — the time stamp for the ISP for this record.	
ISPPKTVN	Image Status Packet Version — 001.195 for all on-orbit observations	
HSQFGSN	Filtergram sequence number from the ISP (used to match the ISP to the TLM packets)	
HSQFGID	Filtergram ID read from the ISP. Identifies the filtergram parameters.	
HCAMID	Camera light path identifer. 0 & 1 for dark frames, cameras 1 & 2 respectively. 2 & 3 for light exposures, cameras 1 & 2 respectively.	
HSHIEXP	Commanded exposure. For any calculations requiring the exposure time, the actual exposure EXPTIME should be used.	

Keyword	Description	Reference
HOBITSEC	Seconds (in TAI) of the shutter move start time.	
HOBITSS	Subseconds of the shutter move start time.	
HWLTNSET	Image Stabilization System (ISS) loop status. CLOSED means the ISS is stabilizing the image and science quality images are being taken. OPEN means the image is not being stabilized.	
HSQSTATE	State of the sequencer. Can be IDLE, SELECTING, or PROCESSING.	
HSEQERR	Error message of the last sequencer error.	
HFLREFTM	Current framelist reference start time.	
HFLRELTM	Time in milliseconds from the current framelist reference start time (HFLREFTM).	
HFLID	Framelist identification number.	
HOBLSTID	Observation list identification number.	
HFLPSITN	Position number of the current frame in the framelist.	
HSQFCNT	The number of frames taken since the start of the sequence.	
HFLLNGTH	Number of frames in the current framelist.	
HFLRPTCT	Number of repeats of the active framelist specified.	
HFLRPTNM	Repeat number of the active framelist.	
HFLSKPCT	Number of candence periods to skip for the active framelist.	
HFTSACID	Active Framelist Timeline Specification ID.	
HFTSCDMK	Number of cadence periods ellapsed since FTS start.	
HFTSINFO	FTS status info.	
HSQEIDX	Current exposure index; references the exposure setting table.	App D.5
HIMGCFID	Current image configuration ID number.	App D.6
HCFTID	Current focus setting ID	App D.4
HPLTID	Current polarization setting ID	App D.2
HWLTID	Current wavelength tuning position ID	App D.3
HWLSTIDX	Current active wavelength tuning set index	App D.3
HGP1RGST	General purpose register #1 (set by command).	
HGP2RGST	General purpose register #2 (set by command).	
HSHMIOPB	Shutter timer open value for the bottom sensor.	
HSHMIOPM	Shutter timer open value for the middle sensor.	
HSHMIOPT	Shutter timer open value for the top sensor.	
HSHMICLB	Shutter timer close value for the bottom sensor.	
HSHMICLM	Shutter timer close value for the middle sensor.	
HSHMICLT	Shutter timer close value for the top sensor.	

Keyword	Description	Reference
HCF1ENCD	Position of focus wheel 1. Return value from the CF1 encoder.	App D.4
HCF2ENCD	Position of focus wheel 2. Return value from the CF2 encoder.	App D.4
HPS1ENCD	Position of polarization selector 1. Return value from the PS1 encoder.	
HPS2ENCD	Position of polarization selector 2. Return value from the PS2 encoder.	
HPS3ENCD	Position of polarization selector 3. Return value from the PS3 encoder.	
HWT1ENCD	Position of the Lyot tunable element wavelength tuning selector. Return value of the WT1 encoder.	
HWT2ENCD	Position of the wideband Michelson wavelength tuning selector. Return value of the WT2 encoder.	
HWT3ENCD	Position of the rotating polarizer. Return value of the WT3 encoder.	
HWT4ENCD	Position of the narrowband Michelson wavelength tuning selector. Return value of the WT4 encoder.	
HCF1POS	Commanded position of focus wheel 1.	
HCF2POS	Commanded position of focus wheel 2.	
HPL1POS	Commanded position of polarization selector 1.	
HPL2POS	Commanded position of polarization selector 2.	
HPL3POS	Commanded position of polarization selector 3.	
HWL1POS	Commanded position of the Lyot wavelength tuning selector.	
HWL2POS	Commanded position of the wideband Michelson wavelength tuning selector.	
HWL3POS	Commanded position of the rotating polarizer.	
HWL4POS	Commanded position of the narrowband Michelson wavelength tuning selector.	
Level 1 specific keywords.		
OSCNMEAN	Mean value of the pixels in the overscan rows.	
OSCNRMS	RMS value of the pixels in the ovserscan rows.	
FLAT_REC	Pointer to the flafield that was applied to the image segment.	
NBADPERM	Number of known permanently bad pixels on the camera.	
NBADTOT	Total number of bad pixels — is the sum of the permamently bad pixels and the pixels flagged as cosmic ray hits.	
Pointing and location keywords. Source: Master pointing table and FDS products.		

Keyword	Description	Reference
MPO_REC	A pointer to the Master Pointing Table (MPT) record appropriate for this record.	
INST_ROT	The angular offset between the spacecraft's orrientation and the camera.	
IMSCL_MP	Image scale from the Master Pointing Table.	
X0_MP	Horizontal center of the solar disk on the image from the Master Pointing Table.	
Y0_MP	Vertical center of the solar disk on the image from the Master Pointing Table.	
RSUN_LF	Radius of the Sun on the image in pixels as measured by the limb finder.	Sec 5.2.2.1
X0_LF	Horizontal center of the solar disk on the image as determined by the limb finder	Sec 5.2.2.1
Y0_LF	Horizontal center of the solar disk on the image as determined by the limb finder	Sec 5.2.2.1
ASD_REC	Pointer to the Ancillary Science Data packet for this record.	
SAT_Y0	Position of solar center with respect to the SDO -Y axis, in arcseconds.	
SAT_Z0	Position of solar center with respect to the SDO Z axis, in arcseconds.	
SAT_ROT	Angle of the solar north pole with respect to the SDO X axis, in degrees.	
ACS_MODE	Status of the spacecraft's Attitude Control System. Can be SCIENCE for fine guidance mode, or INERTIAL. The ISS is not used when the spacecraft is in INERTIAL pointing mode, so science quality data are not taken.	
ACS_ECLP	Flag set by the ACS for Earth or Lunar transits.	
ACS_SUNP	Flag set by the ACS when the Sun is present in the spacecraft's sun sensors.	
ACS_SAFE	Flag set when the spacecraft has indicated it will immenently enter a safe hold (HMI is powered off during a safe hold).	
ACS_CGT	ID of the guide telescope used by the ACS.	
ORB_REC	Pointer to the orbit vector series and record.	
DSUN_REF	Reference distance to the Sun: 1AU in meters.	
DSUN_OBS	Actual distance from the spacecraft to the Sun	
RSUN_REF	Reference radius of the sun, 6.96×10^8m.	
RSUN_OBS	Apparent radius of the Sun. Computed from DSUN_OBS and RSUN_REF.	

Keyword	Description	Reference
GAEX_OBS	Geocentric Inertial X position in meters.	
GAEY_OBS	Geocentric Inertial Y position in meters.	
GAEZ_OBS	Geocentric Inertial Z position in meters.	
HAEX_OBS	Heliocentric Inertial X position in meters.	
HAEY_OBS	Heliocentric Inertial Y position in meters.	
HAEZ_OBS	Heliocentric Inertial Z position in meters.	
OBS_VR	Velocity of the spacecraft toward the Sun, in m s^{-1}.	
OBS_VW	Velocity of the spacecraft in the solar-west direction, in m s^{-1}.	
OBS_VN	Velocity of the spacecraft in the solar-north direction, in m s^{-1}.	
CRLN_OBS	Carrington longitude of the center of the solar disk seen by SDO.	
CRLT_OBS	Carrington latitude of the cetner of the solar disk seen by SDO.	
CAR_ROT	Carring rotation number of CRLN_OBS.	
HGLN_OBS	Stonyhurst heliographic longitude of the observer.	
HGLT_OBS	Stonyhurst heliographic latitude of the observer.	
Level 1.5 (LOS Observables) keywords.		
T_REC	Target time for which the given record was generated.	
CADENCE	Cadence of the target times for this series.	
BUNIT	The physical unit for the given observable.	
DATASIGN	The sign of the observable quantity with respect to the Sun center.	
CONTENT	Name of the type of data product in the record.	
HISTORY	String containing information about the record. Contains the polynomial coefficients for the velocity correction.	
COMMENT	String containing further information about the record.	
SOURCE	Pointer to every level 1 record used in the calculation of the given record.	
SATVALS	Number of pixels with saturated values.	
QLOOK	Flag for Near Real Time data. If set, record is NRT data. Otherwise the record is a definitive product.	
CAL_FSN	Filtergram sequence number of the first filtergram used to produce the look-up table used.	
LUTQUERY	Pointer to the look-up table used to produce the observables.	
TSEL	Temperature (C) of the polarization selectors.	
TFRONT	Temperature (C) of the front telescope mounting ring.	

Keyword	Description	Reference
TINTNUM	Number of points used in the temporal interpolation.	
SINTNUM	Number of points used in the spatial interpolation.	
DISTCOEF	Pointer to the distortion coefficients used to correct the input filtergrams.	
ROTCOEF	Pointer to the differential rotation coefficients used to de-rotate the filtergrams.	
ODICOEFF	Order of the distortion coefficients.	
OROCOEFF	Order of the differential rotation coefficients.	
POLCALM	Method used by the polarization calibration subroutine. Currently only one method implemented, so this is always 1.	
CODEVER0	Version of the LOS observables code used to produce the data.	
CODEVER1	Version of the gapfilling subroutine used to produce the data.	
CODEVER2	Version of the temporal interpolation subroutine used to produce the data.	
CODEVER3	Version of the polarization calibration subroutine used to produce the data.	

E.2   Quality Keywords

Every filtergram and observables record has a QUALITY keyword that identifies known issues or problems with that record. Table 20 gives a list of isses and problems that are checked for. When present, the associated bit is set in the QUALITY keyword. A record with QUALITY=0 has no known issues and is considered science quality.

Bit	Name	Description
		Level 0 Quality Bits
0x01	Q_OVFL	Overflow flag set.
0x02	Q_HDRERR	Header error flag set.
0x04	Q_CMPERR	Compression error in image.
0x08	Q_LPXERR	Last pixel error.
0x10	Q_NOISP	No Image Status Packet found.
0x20	Q_MISSI	Missing image.
0x40	Q_CORRUPT	Corrupt image.
0x80	Q_INVALTIME	HOBITSEC = 0 (T_OBS = 1958.01.01_00:00:00_UTC)
0x100	Q_MISS0	MISSVALS > 0
0x200	Q_MISS1	MISSVALS > 0.01*TOTVALS
0x400	Q_MISS2	MISSVALS > 0.05*TOTVALS

Bit	Name	Description
0x800	Q_MISS3	MISSVALS > 0.25*TOTVALS
0x1000	Q_MISCONFIG	Instrument miss-configured.
0x2000	Q_INSTR_ANOM	Instrument anomaly.
0x8000	Q_CAM_ANOM	Camera anomally.
0x10000	Q_DARK	Dark image.
0x20000	Q_ISSOPEN	ISS loop open (HWLTNSET = 'OPEN').
0x40000	Q_HCF1ENCD	Focus/Cal Motor 1 Error - HCF1ENCD $\neq$ HCF1POS $\pm$ 1
0x80000	Q_HCF2ENCD	Focus/Cal Motor 2 Error - HCF2ENCD $\neq$ HCF2POS $\pm$ 1
0x100000	Q_HPS1ENCD	Polarization MTR 1 Error - HPS1ENCD $\neq$ HPL1POS $\pm$ 1 %240
0x200000	Q_HPS2ENCD	Polarization MTR 2 Error - HPS2ENCD $\neq$ HPL2POS $\pm$ 1 %240
0x400000	Q_HPS3ENCD	Polarization MTR 3 Error - HPS3ENCD $\neq$ HPL3POS $\pm$ 1 %240
0x800000	Q_HWT1ENCD	Wavelength Motor 1 Error - HWT1ENCD $\neq$ HWL1POS $\pm$ 1 %240
0x1000000	Q_HWT2ENCD	Wavelength Motor 2 Error - HWT2ENCD $\neq$ HWL2POS $\pm$ 1 %240
0x2000000	Q_HWT3ENCD	Wavelength Motor 3 Error - HWT3ENCD $\neq$ HWL3POS $\pm$ 1 %240
0x4000000	Q_HWT4ENCD	Wavelength Motor 4 Error - HWT4ENCD $\neq$ HWL4POS $\pm$ 1 %240
0x40000000	Q_REOPENED	Image reopened during reconstruction; no impact on data quality except in rare cases where telemetry retransmission may have caused inflated NPACKETS value
0x80000000	Q_MISSALL	Data are completely missing.

Level 1 Quality Bits

Bit	Name	Description
0x01	Q_NOFLAT	Flatfield not available or error.
0x02	Q_NOORB	Orbit data not available or error.
0x04	Q_NOASD	Ancillary Science Data packet not available or error.
0x08	Q_NOMPD	Master Pointing Table data not available or error.
0x10	Q_NOLIMB	Limb fit error.
0x20	Q_INSTR_ANOM1	Instrument anomaly.
0x40	Q_MISCONF1	Instr Miss-configured. Inherited from level 0.
0x80	Q_CAM_ANOM1	Camera Anomaly.

Bit	Name	Description
0x100	Q_1_MISS0	MISSVALS > 0
0x200	Q_1_MISS1	MISSVALS > 0.01*TOTVALS
0x400	Q_1_MISS2	MISSVALS > 0.05*TOTVALS
0x800	Q_1_MISS3	MISSVALS > 0.25*TOTVALS
0x1000	Q_NOACS_SCI	Attitude Control System (ACS) in not in science mode.
0x2000	Q_ACS_ECLP	Eclipse flag set by ACS.
0x4000	Q_ACS_SUNP	Sun not present in ACS sensors.
0x8000	Q_ACS_SAFE	Safe hold immanent.
0x10000	Q_IMG_TYPE	Dark image.
0x20000	Q_LOOP_OPEN	Image Stabalization System loop is open.
0x40000	Q_CAL_IMG	Calibration image.
0x80000	Q_CALM_IMG	CALMODE image.
0x400000	Q_THERM_ RECOV	HMI thermal recovery (set after eclipses).
0x800000	Q_LUNAR_ TRAN	Lunar transit.
0x40000000	Q_NRT	Near Real Time (NRT) mode. Also known as quicklook.
0x80000000	Q_MISSALL	Image not available.
	Level 1.5 Quality Bits	
0x20	Q_POORQUALITY	Poor quality: may be due to eclipse, lunar transit, thermal recovery, open ISS, or other issues.
0x40	Q_LARGEFTSID	HFTSACID of target filtergram > 4000, which adds noise to observables.
0x80	Q_TEMPERROR	Code error discovered, will be corrected in later versions, see notes at `http://jsoc2.stanford.edu/doc/data/ hmi/Quality_Bits`.
0x100	Q_ECLIPSE	At least one level 1 record was taken during an eclipse.
0x200	Q_NOCOEFF KEYWORD	Could not read the keywords of the polynomial coefficient series.
0x400	Q_NOCOSMICRAY	Some cosmic-ray hit lists could not be read for the level 1 filtergrams.
0x800	Q_LIMBFITISSUE	Some level 1 records were discarded because R_SUN, and/or CRPIX1/CRPIX2 were missing or too different from the median value of the other level 1 records.
0x1000	Q_NOGAPFILL	The code could not properly gap-fill all of the level 1 filtergrams.

Bit	Name	Description
0x2000	Q_NOTEMP	Could not read the temperatures needed for polarization calibration (default temperatures are used).
0x4000	Q_ISSTARGET	The ISS loop was OPEN for one or several filtergrams used to produce the observable.
0x8000	Q_LOW KEYWORDNUM	Some keywords (especially CROTA2, DSUN_OBS, and CRLT_OBS) could not be interpolated properly at target time, but a closest-neighbour approximation or an extrapolation was used.
0x10000	Q_LOW INTERPNUM	the number of interpolation points (for temporal interpolation) was not always as high as expected, AND/OR 2 interpolation points were separated by more than the cadence
0x20000	Q_MISSINGLEV1P	Not enough level 1p (polarization-calibrated filtergrams) records to produce an observable (too many level 1 records were missing or corrupted)
0x40000	Q_INTERPOLATION FAILED	The temporal interpolation routine failed.
0x80000	Q_NOTENOUGH INTERPOLANTS	Not enough interpolation points for the temporal interpolation at a given wavelength and polarization (too many level 1 records were missing or corrupted).
0x100000	Q_NOLOOKUP KEYWORD	Could not read the keywords of the look-up tables for the MDI-like algorithm (the MDI-like algorithm cannot be used).
0x200000	Q_NOLOOKUP RECORD	Could not find a record for the look-up tables for the MDI-like algorithm (the MDI-like algorithm cannot be used).
0x400000	Q_MISSING KEYWORDLEV1P	Could not read some needed keywords in the level 1p (polarization-calibrated filtergrams) record (too many lev 1 records were missing or corrupted and the corresponding level 1p record is unusable).
0x800000	Q_WRONG WAVELENGTH-NUM	The number of wavelengths in the level 1d (combined filtergrams) records is not correct (issue with the framelist, or too many level 1 records were missing or corrupted).

Bit	Name	Description
0x1000000	Q_MISSING KEYWORDLEV1D	Could not read some needed keywords (like FID) in the level 1d (combined filtergrams) data (too many lev 1 records were missing or corrupted and the corresponding level 1d record is unusable).
0x2000000	Q_MISSINGLEV1D	Not enough level 1d (combined) filtergrams to produce an observable (too many level 1 records were missing or corrupted).
0x4000000	Q_WRONG TARGET	The target filtergram does not belong to the current framelist (there is something wrong either with the framelist or the target filtergram).
0x8000000	Q_WRONG CADENCE	The cadence corresponding to the framelist run at the required time does not match the expected value provided by user (could be an error from user, or an issue with the framelist).
0x10000000	Q_NOFRAMELIST INFO	Could not figure out which observables framelist was used, or the framelist run for the required time range is not an observables framelist.
0x20000000	Q_NOINTERPOLATED KEYWORDS	Could not interpolate some keywords at target time because some level 1 records are missing or corrupted.
0x40000000	Q_TARGET FILTERGRAM MISSING	No target filtergram was found near target time.
0x80000000	Q_NODATA	No LOS observables were produced (record created, but no data segment). Most keywords have default value.

Table 20: Quality bits and their meanings for level 0, level 1 , and l.5 records.

E.3   Calibration Version Keywords

Keywords describing the HMI calibration version have been included in level-1 data (CALVER32) and higher level products (CALVER64) starting in August 2012. This keyword is a set of fields consisting of single hexidecimal digits. Each nibble has a meaning described in the following table.

Field	Bits	Mask		Notes
0	0-3	0x0f	HFCORRVR	Height-of-formation code version used to find disk center. Vers 2 for all data to date.
1	4-7	0xf0	CROTA2VR	Version of CROTA2 in the Master pointing table. Vers 0 prior to Transit of Venus, then 1.
2	8-11	0xf00		If > 0, then smooth look-up tables were used to produce observables.
3	12-15	0xf000		If > 0, then a correction for non-linearity of the CCDs was applied. See values in table 4.6.4.
4	16-19	0xf0000	Mod L	If greater than 0, Mod L sequence was used. Otherwise Mod C was used. 2: Mod L data processed with incorrect alignment of filtergrams from the two cameras and duplicated 'V' filtergrams. 3: partially corrected Mod L processing with proper alignment but still using only half the available $I \pm V$ filtergrams. Noise levels are higher. 4: Mod L with proper co-allignment and appropriate filtergrams used for all products.
5	20-23	0xf00000		If > 0 then PSF/scattered light deconvolution has been done. If 1, code was CUDA version, if 2, code was C version.
6	24-27	0xf000000		If > 0, rotational flatfield was applied.
7	28-31	0xf0000000		If > 0, then the observer location keywords have been updated.[3]

Table 21: Meaning of each currently used nibble in CALVER32 and CALVER64. For a current list see `http://jsoc.stanford.edu/jsocwiki/CalibrationVersions`.

F   Data Processing Pipeline

The Joint Science Operations Center (JSOC) runs a Science Data Processing facility that ingests, processes, and makes available all data from the HMI instrument, as well as the AIA instrument on SDO, and the IRIS mission.

References

Couvidat, S. et al. (Aug. 2016). "Observables Processing for the Helioseismic and Magnetic Imager Instrument on the Solar Dynamics Observatory". In: *SoPh* 291.7, pp. 1887–1938. DOI: 10.1007/s11207-016-0957-3. arXiv: 1606.02368 [astro-ph.SR].

Couvidat, Sébastien, S. P. Rajaguru, et al. (May 2012). "Line-of-Sight Observables Algorithms for the Helioseismic and Magnetic Imager (HMI) Instrument Tested with Interferometric Bidimensional Spectrometer (IBIS) Observations". In: *SoPh* 278.1, pp. 217–240. DOI: 10.1007/s11207-011-9927-y.

Couvidat, Sébastien, Jesper Schou, et al. (Jan. 2012). "Wavelength Dependence of the Helioseismic and Magnetic Imager (HMI) Instrument onboard the Solar Dynamics Observatory (SDO)". In: *SoPh* 275.1-2, pp. 285–325. DOI: 10.1007/s11207-011-9723-8.

Emilio, M. et al. (Jan. 2015). "Measuring the Solar Radius from Space during the 2012 Venus Transit". In: *ApJ* 798.1, 48, p. 48. DOI: 10.1088/0004-637X/798/1/48.

Fleck, B., S. Couvidat, and T. Straus (July 2011). "On the Formation Height of the SDO/HMI Fe 6173 Å Doppler Signal". In: *SoPh* 271.1-2, pp. 27–40. DOI: 10.1007/s11207-011-9783-9. arXiv: 1104.5166 [astro-ph.SR].

Hoeksema, J. T. et al. (Mar. 2018). "On-Orbit Performance of the Helioseismic and Magnetic Imager Instrument onboard the Solar Dynamics Observatory". In: *SoPh* 293.3, 45, p. 45. DOI: 10.1007/s11207-018-1259-8. arXiv: 1802.01731 [astro-ph.SR].

Kuhn, J. R., H. Lin, and D. Loranz (Oct. 1991). "Gain calibrating NonUniform Image-Array Data Using Only the Image Data". In: *PASP* 103, p. 1097. DOI: 10.1086/132932.

Lucy, L. B. (June 1974). "An iterative technique for the rectification of observed distributions". In: *AJ* 79, p. 745. DOI: 10.1086/111605.

Pesnell, W. Dean, B. J. Thompson, and P. C. Chamberlin (Jan. 2012). "The Solar Dynamics Observatory (SDO)". In: *SoPh* 275.1-2, pp. 3–15. DOI: 10.1007/s11207-011-9841-3.

Pierce, A. K. and C. D. Slaughter (Jan. 1977). "Solar limb darkening. I: lambda lambda (3033 - 7297)." In: *SoPh* 51.1, pp. 25–41. DOI: 10.1007/BF00240442.

Richardson, William Hadley (Jan. 1972). "Bayesian-Based Iterative Method of Image Restoration". In: *Journal of the Optical Society of America (1917-1983)* 62.1, p. 55.

Scherrer, P. H., R. S. Bogart, et al. (Dec. 1995). "The Solar Oscillations Investigation - Michelson Doppler Imager". In: *SoPh* 162.1-2, pp. 129–188. DOI: 10.1007/BF00733429.

Scherrer, P. H., J. Schou, et al. (Jan. 2012). "The Helioseismic and Magnetic Imager (HMI) Investigation for the Solar Dynamics Observatory (SDO)". In: *SoPh* 275, pp. 207–227. DOI: 10.1007/s11207-011-9834-2.

Schou, J., J. M. Borrero, et al. (Jan. 2012). "Polarization Calibration of the Helioseismic and Magnetic Imager (HMI) onboard the Solar Dynamics Observatory (SDO)". In: *SoPh* 275.1-2, pp. 327–355. DOI: 10.1007/s11207-010-9639-8.

Schou, J., P. H. Scherrer, et al. (Jan. 2012). "Design and Ground Calibration of the Helio-seismic and Magnetic Imager (HMI) Instrument on the Solar Dynamics Observatory (SDO)". In: *SoPh* 275.1-2, pp. 229–259. DOI: 10.1007/s11207-011-9842-2.

Tepper-García, Thorsten (July 2006). "Voigt profile fitting to quasar absorption lines: an analytic approximation to the Voigt-Hjerting function". In: *MNRAS* 369.4, pp. 2025–2035. DOI: 10.1111/j.1365-2966.2006.10450.x. arXiv: astro-ph/0602124 [astro-ph].

Toro Iniesta, J. C. del (2003). *Introduction to spectropolarimetry*. Cambridge ; New York: Cambridge University Press.

Wachter, R. et al. (Jan. 2012). "Image Quality of the Helioseismic and Magnetic Imager (HMI) Onboard the Solar Dynamics Observatory (SDO)". In: *SoPh* 275.1-2, pp. 261–284. DOI: 10.1007/s11207-011-9709-6.